Journal of Geophysical Research: Oceans

RESEARCH ARTICLE
10.1029/2018JC013985

Flow Regimes and Adjustment to Wind-Driven Motions in Lake Pontchartrain Estuary: A Modeling Experiment Using FVCOM

Chunyan Li[1], **Wei Huang**[1], **Changsheng Chen**[2,3], **and Huichan Lin**[2]

[1]Department of Oceanography and Coastal Sciences, Louisiana State University and A. & M. College, Baton Rouge, LA, USA, [2]School of Marine Science and Technology, University of Massachusetts Dartmouth, New Bedford, MA, USA, [3]International Center for Marine Studies, Shanghai Ocean University, Shanghai, China

Key Points:
- Seiche generated by wind is dissipated in two to three cycles, adjusting the system to a new balance, leading to a quasi steady state
- Subtidal cross bay slopes are determined by local wind, generating strong coastal currents; neglecting rotation only produces 0.3% error
- Bottom flows are counterwind, broad, and uniform; Engelund model is applicable for circulation

Supporting Information:
- Supporting Information S1
- Data Set S1

Correspondence to:
C. Li,
cli@lsu.edu

Citation:
Li, C., Huang, W., Chen, C., & Lin, H. (2018). Flow regimes and adjustment to wind-driven motions in Lake Pontchartrain Estuary: A modeling experiment using FVCOM. *Journal of Geophysical Research: Oceans*, *123*, 8460–8488. https://doi.org/10.1029/2018JC013985

Received 16 MAR 2018
Accepted 2 NOV 2018
Accepted article online 8 NOV 2018
Published online 25 NOV 2018

Abstract Lake Pontchartrain is a brackish estuary and restricted lagoon in the microtidal northern Gulf of Mexico. Using a validated Finite Volume Community Ocean Model (FVCOM), we study the flow regimes and wind-driven adjustment of circulation in this system. It is found that tidal currents are only significant in the eastern end near the open boundary. Local wind inside the estuary is important in driving the circulation including coastal currents. Numerical experiments confirm that the subtidal wind-driven flow is in a quasi-steady balance between wind stress and surface slope. Our results show that the adjustment of surface level inside the system to a sudden change in wind is a transient seiche, which dissipates within two to three cycles, each lasting ~3 hr. After the oscillations, the system reaches a new equilibrium. We show in theory that this is a damped oscillation and as wind changes, an adjustment to a new equilibrium goes much faster than a complete tidal period. This leads to the quasi steady state balance of subtidal wind-driven flows with essentially no phase lag with wind even though wind changes with time continuously. Wind-induced circulation behaves differently from the Csanady model with Earth rotation but similar to the prismatic lake model of Engelund without Coriolis: The coastal and shallow regions tend to have flows in the direction of wind, while the interior and deeper waters have return flows against the wind especially in bottom layer. The surface flow may not be in the direction of wind, while the bottom usually has broad and uniform counter wind flows.

Plain Language Summary In a choked or restricted shallow lagoon, wind-driven flows are confirmed to be a surprising quasi steady state. Numerical experiments show that any change in wind would produce a hydrodynamic perturbation in the form of seiche that dissipates quickly in two to three cycles, leading to a fast return to a new equilibrium or quasi steady state. This warrants examination of wind-driven flows at constant speed for different scenarios (wind from different directions) and not to worry too much about the temporal variation of wind or history of wind. Earth rotation in such system is found to be negligible for wind-driven circulations: The experiment shows that the relative error is only 0.3% if Coriolis force is turned off for Lake Pontchartrain.

1. Introduction

Estuaries and coastal lagoons can be significantly influenced by tides (e.g., de Brito et al., 2018; Waterhouse et al., 2011) and winds (e.g., Garvine, 1985; Wilson et al., 1985). Given enough data, tides can be predicted using harmonic analysis (e.g., Boon, 2004). While wind can also produce significant flows, mostly at frequencies lower than those of tides—the so-called subtidal flows (Valle-Levinson et al., 2007; Wong & Wilson, 1984), the effect is more challenging to predict because weather is much more variable and less regular than tides. Among the weather events, there are the hurricanes or cyclones (e.g., Kumar et al., 2017; Weaver, Johnson et al., 2016), winter storms (e.g., Beardsley et al., 2013), atmospheric fronts (e.g., Feng & Li, 2010; Li et al., 2018; Walker & Hammack, 2000; Weaver, Taeb et al., 2016), and sea breezes (Mohanty & Panda, 2009). The effect of wind has been recognized and studied in various estuaries and lagoons (e.g., Elliott, 1978; Smith, 1985; Sternberger, 1983; Weisberg, 1976; Winant et al., 2014; Wong, 1994; Wong & Moses-Hal, 1998; Wong & Wilson, 1984). Sometimes local wind effect and remote wind effect are studied separately (e.g., Casares-Salazar & Mariño-Tapia, 2016; Feng & Li, 2010; Garvine, 1985; Huang & Li, 2017; Jordi et al., 2011). Here the terminology *remote wind effect* is meant for all the effects of the weather system (except that from local wind stress) that is propagated into the region in the form of an open boundary water level change. It is an integrated water level variation due to a weather system affecting the region. Unlike the wind-driven motions

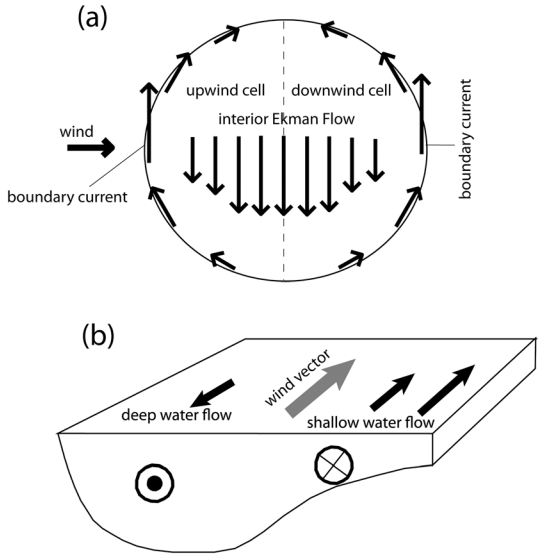

Figure 1. Schematic plots of wind-driven circulation in the (a) Csanady (1968) model and (b) Engelund (1973) model.

in offshore or open ocean waters (e.g., Flores et al., 2017; Horner-Devine et al., 2015), estuaries are semienclosed (Cameron & Pritchard, 1963; Hansen & Rattray, 1965, 1966) and lagoons can be more limited in exchange with the coastal ocean (Kjerfve, 1986; Kjerfve & Magill, 1989) and may even have multiple openings (Duran-Matute et al., 2016; Herrling & Winter, 2015; Jia & Li, 2012; Li, 2013). The constrictions of such system at entrance can act as low-pass filters that diminish tidal influence into the basin (Fernandes et al., 2004) or change the fortnightly tidal phases (Hill, 1994).

Wind stress can cause significant water setup at coast (e.g., Betancourt et al., 2008; Moller et al., 1996). It has been found that in a lagoon, wind can produce a coastal current based on the orientation of the coastline and the direction of wind. The effect of wind can produce two-layered horizontal flows in the vertical (Chubarenko et al., 2012; Lin et al., 2016), allowing return flows at bottom, as well as vertical circulations (De Marchis et al., 2012; Lawson et al., 2007). An important effect of wind is to generate abnormal water level variations or storm surges (de Oliveira et al., 2009), which will affect exchanges with outside waters through various mechanisms (Umgiesser et al., 2014, 2016; Valle-Levinson et al., 2001; Yuk & Aoki, 2009).

As extreme examples of enclosed or restricted waterbodies (Kjerfve, 1986), wind-driven circulations for large lakes have been studied with theoretical models (e.g., Cheng et al., 1976; Csanady, 1968, 1982). For a waterbody to be *large*, it needs to have a spatial scale greater than the external Rossby deformation radius $R = \sqrt{gh}/f$, in which g, h, and f are the gravitational acceleration, mean water depth, and Coriolis parameter, respectively. By neglecting bottom friction, Csanady (1968, 1982) developed an analytical model for a circular-shaped basin allowing Earth rotation and solved the steady state barotropic wind-driven circulation on an f plane. The circulation consists of two cells, with the interior having crosswind flows in the direction of the Coriolis force. At the downwind and upwind ends of the basin along the coastlines, return flows are established in the opposite direction of Coriolis force (Figure 1a). This can be viewed as an esthetic extension of the Ekman's solution in an infinite ocean without a lateral boundary. The return flows opposite of the interior Ekman transport at the end walls are limited to near the coast, which are called by Csanady (1982) the coastal boundary layer.

However, these restricted estuaries or enclosed large lakes are rare. With the Great Lakes (i.e., Lakes Superior, Michigan, Erie, Ontario, and Huron) of the United States as examples, take an averaged depth to be ~100 m, latitude 45°, the external Rossby radius of deformation would be ~300 km. The lengths of the Great Lakes are comparable or slightly larger than R (scale ratio L/R around 1 but less than 2), their widths are all smaller than R ($L/R < 1$), much smaller than the one used in Csanady (1982), in which a scale ratio of 15 is chosen for the calculation of the solution. For restricted estuaries and lagoons, they are usually much smaller than the Great Lakes. For problems with stratification, this view of course will have to be modified. Here, however, we are focusing only on barotropic problems as our subject is of shallow water in a restricted lagoon and the main interest is wind-driven flows such that, to the first order of approximation, only well-mixed water is involved. In addition, it is reminded that the Csanady model, albeit intuitive and useful for understanding of wind-driven flows, neglects bottom stress, and that is why the crosswind flow is 90° to the right of the wind vector, just like an idealized Ekman transport.

Interestingly, there is a contrasting simple model that includes friction but neglects Coriolis. The model is proposed by Engelund (1973) for a prismatic lake. An analytic solution shows that the flow is in the direction of wind in shallow waters but against the wind in deep waters. For a closed basin, the deep water experiences return flows, forming a cell or cells, depending on the actual bathymetry (Figure 1b). A coastal current can form in the direction of wind because coastal waters are usually shallower than offshore water. At the same time, the deep water can have either weaker currents in the direction of wind or return flows if the basin is closed (without a major outlet downwind). This is essentially a torque or vorticity issue—when the shallow water and deep water are applied with a constant surface (wind) stress, the shallower water

will accelerate faster as it has less inertia. As a result, a vorticity is produced and the water will tend to *rotate* such that particles in shallow water will tend to move with the wind and those in deep water against the wind.

There are many shallow water systems that are choked or restricted (Kjerfve, 1986; e.g., Lake Pontchartrain Estuaries, LPE) but not large because usually the scale ratio L/R is much smaller than 1. They have only limited connections to the coastal ocean through narrow tidal passes. Two-dimensional numerical model experiments (Hamilton et al., 1982; Haralampides, 2000; Signell & List, 1997) for wind-driven flows in LPE have shown results consistent with that from Engelund (1973). More recent studies (e.g., Gibbs et al., 2016; Lin et al., 2016) seem to suggest that the mechanism shown by Engelund (1973) is more important in these smaller systems. Particularly, the work of Lin et al. (2016) uses a numerical model experiment in the Calcasieu Lake estuary in the northern Gulf of Mexico to study winter time circulation driven by cold fronts (Chaney & Stone, 1996; Feng & Li, 2010; Keen, 2002; Li et al., 2011; Moeller et al., 1993; Pepper & Stone, 2004; Roberts et al., 1989, 2005; Walker, 1996; Walker & Hammack, 2000). The study shows that wind-driven flows are downwind in shallow waters balanced by return flows against wind in the deep ship channel that can facilitate saltwater intrusion. In a recent study (Huang & Li, 2017), a three-dimensional Finite Volume Community Ocean Model (FVCOM) is used for LPE to study cold front weather-induced flows through multiple inlets. It is found that the overall water level variation in the lake is controlled by remote wind effect while the water surface slope variation is mainly determined by local wind stress. In addition, there is a quasi steady state momentum balance that apparently simplifies the understanding of the dynamics quite dramatically: The surface slope inside the almost enclosed estuary is under a quasi steady state balance between the wind stress and the surface slope-induced pressure gradient force. Motivated by these new findings, we conduct a numerical experiment using a three-dimensional wind-driven circulation model to determine the flow regimes in the LPE and the fundamental reason of the quasi steady state.

Based on the above discussion, the objectives of this study are to (1) conduct a three-dimensional numerical model experiment in the LPE to determine the flow regimes, identifying if there is any region dominated by wind or tide and if there is any coastal current; (2) conduct a numerical experiment for wind-driven flows in the system to establish surface and bottom flow patterns that can be evaluated against theories for a better understanding of the mechanism of wind-driven flows; and (3) experiment with the wind-driven adjustment problem (Gill, 1982) in such a system and determine the mechanism of quasi steady state response. In addition, we will also examine the effect of Earth rotation by comparing results from the models with and without Coriolis force. In the next section, the study site is introduced. In section 3, the numerical model experimental design is described. Section 4 discusses the model results, followed by section 5 with conclusions.

2. Study Site

LPE is a large, shallow, and low-salinity estuary located north of New Orleans (Figure 2). It has a width of ~66 km in the east-west directions and 40 km in the north-south directions. The mean depth of the estuary is only about 3.7 m (Junot et al., 1983). Its external Rossby Deformation Radius is thus about 80 km. The freshwater discharge is in the north and west from a few small rivers including Tchefuncte and Tangipahoa Rivers (Figure 2). Additional freshwater discharge is from the city runoff along the southern shore, and the Rigolets from the Pearl River discharge (e.g., Haralampides, 2000). The salinity inside LPE is mostly low, between 4 and 9 PSU, although earlier studies reported smaller salinity ranges such as 1–5 PSU (Sikora & Kjerfve, 1985). It had three narrow tidal channels connecting the coastal ocean: Water with higher salinity comes into the estuary by tidal currents and wind-driven flows via these channels (Chilmakuri, 2005; Chuang & Swenson, 1981; Georgiou, 2002; Georgiou & McCorquodale, 2002; Haralampides, 2000; Sikora & Kjerfve, 1985; Swenson & Chuang, 1983). The channel to the northeast is the 430-m-wide Rigolets (marked with R in Figure 2), which leads to the mouth of the Pearl River, which may deliver significant amount of fresh water into the Mississippi Sound. The Rigolets therefore acts as a conduit to move the brackish water in and out of the system. Between Lake Pontchartrain and Lake Borgne, there is another tidal pass southwest of the Rigolets of about 270 m in width, the Chef Menteur (marked with CM in Figure 2). In the southeast of the LPE, there was the third tidal channel, Industrial Canal or Inner Harbor Navigational Channel connected to the Mississippi River Gulf Outlet, which was a manmade navigation channel, with a width of ~90 m. These

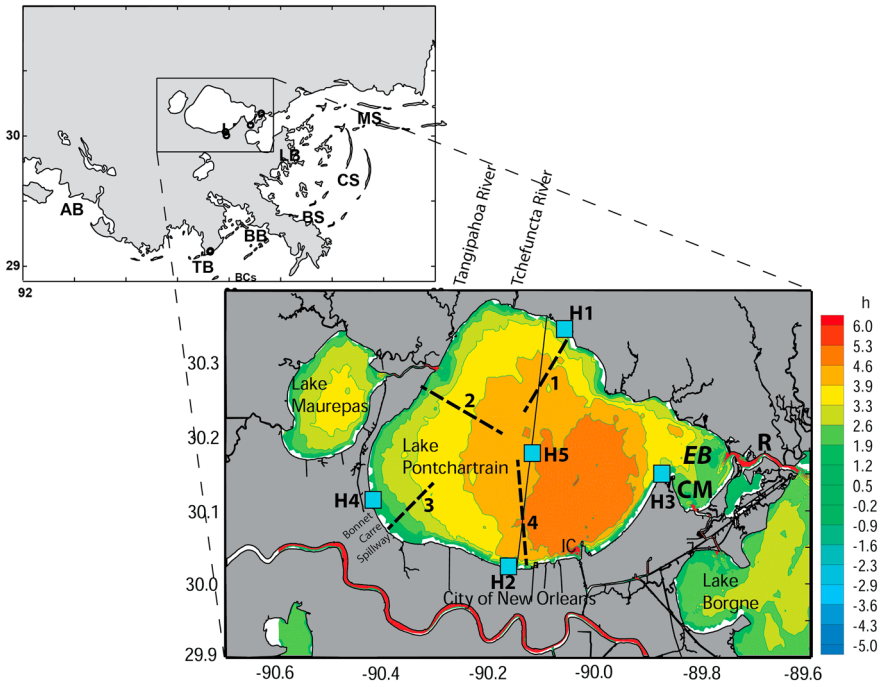

Figure 2. Study site—Lake Pontchartrain Estuary. Noted on the map are locations for the Bonnet Carré Spillway, Industrial Canal (IC) entrance to Lake Pontchartrain Estuary, Chef Menteur (CM) tidal pass, Rigolets (R) tidal pass, eastern bay (EB), causeway (solid line across the central lake north-south), and four locations of pressure sensor deployment. The dashed lines numbered as 1, 2, 3, and 4 are selected transects for analyzing vertical profiles of flows from the model.

three channels provided limited exchange of ocean water with the large lake. After Hurricane Katrina, the north end of the third channel (Industrial Canal) was closed by a floodgate—a construction started in the Fall of 2010 and finished in the middle 2012. The connection to the coastal ocean makes the lake an estuary (Sikora & Kjerfve, 1985) but can also be classified as a restricted lagoon (Kjerfve, 1986).

LPE is bounded by the Mississippi River to its south, which flows almost parallel to its south boundary for about the entire width of the lake—about 60 km. LPE has also a controlled connection with the Mississippi River through the manmade Bonnet Carré Spillway, which is a more than 3-km-wide low-lying rectangular passage for diverting Mississippi River water into the LPE during extreme spring flood conditions. Since its construction in the early twentieth century, Bonnet Carré Spillway has only been opened a total of 12 times (e.g., Brammer et al., 2007; Kolker et al., 2014; White et al., 2009). For the present numerical experiments, we are only examining the dynamics when this diversion is closed.

3. Model

3.1. FVCOM

In this study, we apply the FVCOM for numerical experiments. FVCOM has been developed by Chen et al. (2003) and it has been applied to numerous coastal and estuarine waters and even global oceans (Aoki & Isobe, 2007; Chen et al., 2007; Huang et al., 2008; Li et al., 2008; Rego & Li, 2009, 2010; Weisberg & Zheng, 2006a, 2006b). This model combines the advantages of finite element method using unstructured triangular grids so that it can match the coastline much better than a model with curvilinear structured grids and that of the finite difference method using simple discrete schemes for the differential equations so that volume conservation can be easily enforced for stable integrations over a long time period. In our study, we use the fully nonlinear 3-D FVCOM with tidal forcing implemented from the open boundary of the domain (Figure 3).

The governing equations include those for momentum and mass conservations, and temperature, salinity, and density, as follows (Chen et al., 2003):

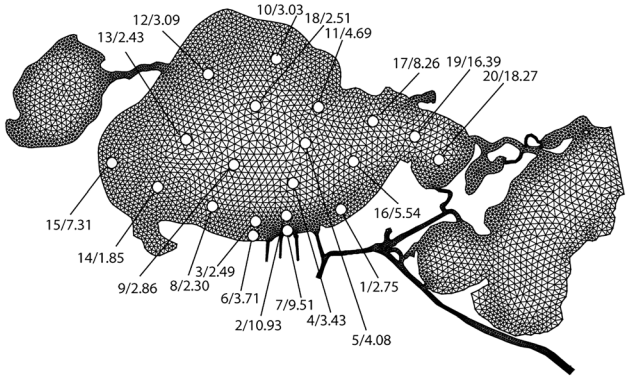

Figure 3. Model grid and selected grid points for analysis of model result offlow time series. The first number is the serial number of selected points, and the second number after the slash is the diurnal tidal velocity amplitude in centimeters per second.

$$\frac{\partial u}{\partial t}+u\frac{\partial u}{\partial x}+v\frac{\partial u}{\partial y}+w\frac{\partial u}{\partial z}-fv=-\frac{1}{\rho_0}\frac{\partial P}{\partial x}+\frac{\partial}{\partial z}\left(K_m\frac{\partial u}{\partial z}\right)+F_u, \quad (1)$$

$$\frac{\partial v}{\partial t}+u\frac{\partial v}{\partial x}+v\frac{\partial v}{\partial y}+w\frac{\partial v}{\partial z}+fu=-\frac{1}{\rho_0}\frac{\partial P}{\partial y}+\frac{\partial}{\partial z}\left(K_m\frac{\partial v}{\partial z}\right)+F_v, \quad (2)$$

$$\frac{\partial P}{\partial z}=-\rho g, \quad (3)$$

$$\frac{\partial u}{\partial x}+\frac{\partial v}{\partial y}+\frac{\partial w}{\partial z}=0, \quad (4)$$

$$\frac{\partial \theta}{\partial t}+u\frac{\partial \theta}{\partial x}+v\frac{\partial \theta}{\partial y}+w\frac{\partial \theta}{\partial z}=\frac{\partial}{\partial z}\left(K_h\frac{\partial \theta}{\partial z}\right)+F_\theta, \quad (5)$$

$$\frac{\partial s}{\partial t}+u\frac{\partial s}{\partial x}+v\frac{\partial s}{\partial y}+w\frac{\partial s}{\partial z}=\frac{\partial}{\partial z}\left(K_h\frac{\partial s}{\partial z}\right)+F_s, \quad (6)$$

$$\rho=\rho(\theta,s), \quad (7)$$

where x, y, and z are the three Cartesian coordinates in the east, north, and vertical directions, respectively; u, v, and w are the x, y, and z components of the velocity, respectively; θ, s, and ρ are the potential temperature, salinity, and density, respectively; P is the total pressure of air and water; f is the Coriolis parameter; g is the gravitational acceleration; and K_m and K_h are the vertical eddy diffusion coefficient and thermal vertical diffusion coefficient, respectively. The calculation of K_m and K_h are done with the Mellor and Yamada (1982) level-2.5 turbulent closure scheme, which is modified by Galperin et al. (1988); F_u, F_v, F_θ, and F_s are the diffusion terms for horizontal momentum, thermal diffusion, and salt diffusion. In our experiments, the focus is wind-driven flows, and therefore, no temperature or salinity effect is included as the first-order approximation: The baroclinic mode is turned off, and only barotropic response is studied. In general, inside Lake Pontchartrain the salinity is small (~4 PSU). The overall wind-driven circulation inside the system is mostly barotropic response due to its shallow water (~4 m) except during freshwater diversion periods (roughly once every 10 years) when the 3-km-long Bonnet Carré Spillway was open for a few weeks, generating freshwater plumes. In Chuang and Swenson (1981) a barotropic one-dimensional model was used to study wind-driven subtidal water level variations in Lake Pontchartrain. Though we valid the model by comparing with data (see below), more discussion on the effect of stratification will be done following this work in a separate paper for periods of freshwater diversion when freshwater plumes are present. We use a 3-D model to resolve possible vertical shears of horizontal velocity that a 2-D model cannot.

The surface and bottom boundary conditions are as follows:

$$K_m\left(\frac{\partial u}{\partial z},\frac{\partial v}{\partial z}\right)=\frac{1}{\rho_0}\left(\tau_{sx},\tau_{sy}\right), w=\frac{\partial \zeta}{\partial t}+u\frac{\partial \zeta}{\partial x}+v\frac{\partial \zeta}{\partial y}, at\ z=\zeta(x,y,t) \quad (8)$$

and

$$K_m\left(\frac{\partial u}{\partial z},\frac{\partial v}{\partial z}\right)=\frac{1}{\rho_0}\left(\tau_{bx},\tau_{by}\right), w=-u\frac{\partial H}{\partial x}-v\frac{\partial H}{\partial y}, at\ z=H(x,y) \quad (9)$$

where (τ_{sx}, τ_{sy}) and (τ_{bx}, τ_{by}) are surface wind stresses and bottom stresses. H is the depth, and ζ is the free surface elevation. (τ_{bx}, τ_{by}) are calculated by $C_d\sqrt{u^2+v^2}(u,v)$, where C_d is determined by

$$C_d=\max\left(\frac{k^2}{\ln\left(\frac{z_{ab}}{z_0}\right)^2},0.0025\right), \quad (10)$$

where k is the von Karman constant ~0.4; z_0 is the bottom roughness parameter and is set to be 0.0001 in our case. The drag coefficient C_d is determined by matching a logarithmic bottom layer to the model at a height z_{ab} above the bottom.

Table 1
Finite Volume Community Ocean Model Experimental Design

#	Name of experiment	Wind forcing	Open boundary condition	Description	Purpose
1	Process study experiment	Real wind from NOAA	Tidal elevation	8 Nov to 1 Dec 2005	Identify flow regimes
2	Real case study	No wind	NOAA observed water elevation	Remote wind effect, 12 Feb to 24 Mar 2016	Examine local/remote wind effects
3		Real wind from NOAA	Tidal elevation	Local wind effect, 12 Feb to 24 Mar 2016	
4		Real wind from NOAA	NOAA observed water elevation	Combined effect, 12 Feb to 24 Mar 2016	
5	Constant wind experiment with (#5) or without rotation (#6)	Constant wind with different directions: E, NE, N, NW, W, SW, S, SE. Each direction dominates 15 days.	Water elevation set to be 0	Eight directions of wind with same wind magnitude of 5 m/s. Each wind direction is run for 15 days.	Establish possible circulation patterns under various wind directions.
6					
7	Step wind adjustment experiment	Constant wind with different directions: S, N, E, W, S, W, N. Each direction dominates 15 days (different from Experiments 5 and 6).	Water elevation set to be 0	Direction of wind changes six times with 90° and 180°	Examine the dynamics of adjustment process.

Note. NOAA = National Oceanic and Atmospheric Administration.

The bathymetry used in the model is a combination of bathymetry from previous models (Huang & Li, 2017; Li et al., 2008) and our own observations prior to deployment of instruments and vessel-based surveys (Li et al., 2009, 2010). The model grid has 10,159 triangles covering the entire domain with a total of 5,809 node points (Figure 3). The finest spatial resolution of the triangles is less than 150 m in the southern canals. In the vertical, the water column is divided into 20 layers using the sigma coordinate. The velocity vector is defined on the centroid of each of the 10,159 triangular elements, whereas all the scalars such as the elevation, and depth are defined on each of the 5,809 nodal points.

The integration of the momentum and continuity equations is accomplished by a combination of external and internal modes. The time step for the external mode in our study is set at 1.0 s by the Courant-Friedrichs-Lewy (CFL) condition, while the internal mode time step is set at 5.0 s. There are two open boundaries: One is located on the eastern end, about 28 km from the interior of the lake, connecting Lake Borgne to the coastal ocean, while the other at the southeast end of the Mississippi River Gulf Outlet, more than 45 km away from the lake.

3.2. Model Experimental Design

With FVCOM, seven sets of experiments are done. The first is a process study (Table 1) that uses observed wind for 8 November to 1 December 2005, with the open boundary forced by predicted tidal elevations from 37 tidal constituents obtained from National Oceanic and Atmospheric Administration (NOAA). The maximum tidal range is ~0.6 m. This experiment is done to examine the flow regime differences in different parts of the LPE.

The second, third, and fourth experiments are for simulations using observed wind as forcing for the period of 12 February to 24 March 2016. The difference is that for the second experiment, the open boundary condition is designed for examining the remote wind effects only. The third experiment is designed for examining the local wind only. The fourth experiment is designed for examining the combined effect of remote and local winds. The remote wind experiment does not include any wind stress inside the computational area, while the open boundary uses observed water level variations, which is an integrated effect of tide plus low-frequency water level changed due to the impact of a larger weather system (we call it the remote wind effect for convenience). The local wind experiment includes the wind stress inside the computational area, but the open boundary only includes predicted tidal elevations. The fourth experiment includes both wind stress and the observed water level—it is the real-case simulation that includes both local and remote wind effects.

The fifth and sixth experiments are for constant local winds with and without Coriolis, respectively. In these experiments, wind is specified as a constant in each one of the eight directions: north, south, east, west,

northeast, northwest, southeast, and southwest, respectively. The open boundary is set to have no water level variation, but it allows exchange flows (Table 1). The model is run for 15 days for each wind direction. It reaches equilibrium (steady state) in less than 1 day. The results between days 1–15 are averaged and presented (which can be considered as a steady state solution).

The last experiment is for wind-driven adjustment process. In this experiment, constant winds are supplied at steps of 15 days with sudden change of wind direction in between the steps. Each of the eight steps is a constant wind of 10 m/s from given direction. More specifically, the wind is first supplied as from the south. After 15 days, the wind changes to northerly, which lasts for another 15 days, followed by east, west, south, west, north, and southeast winds, respectively. With this wind function we can examine various scenarios of 90°, 180°, −90°, −180°, and 135° of changes in wind directions. Even though the real wind change is rarely so abrupt, this experiment is aimed at assessing the transient response of LPE to an atmosphere originated perturbation and how long does it take to reach a new equilibrium so to shed light on the quasi steady state discussed in Huang and Li (2017). The adjustment process can also be examined by looking at Experiment 5 after the wind changes directions each time. Experiment 5 has only 45° changes in wind direction; while Experiment 7 has more abrupt changes in wind directions (up to 180°).

Tidal elevation is obtained from two NOAA stations, one is Bay Waveland Yacht, MS (Station ID: 8747437, 30°19.50′N, 89°19.50′W) for the eastern open boundary, and the other is Shell Beach, LA (Station ID: 8761305, 29°52.10′N, 89°40.40′W) for the southern open boundary. Wind data are from a NOAA weather station BYGL1 (8762482) at Bayou Gauche, LA (29°46′36″N 90°25′6″W) for 8 November to 1 December 2005 of Experiment 1 and for simulation period from 12 February to 24 March 2016 of Experiments 2–4.

In all these numerical experiments, an implicit gravity wave radiation boundary condition is specified at the open boundaries to allow the water transport out during ebb tides. To minimize the numerical reflection at the boundary, we also turned on the option of *sponge layer*, which effectively absorbed *reflection* from the boundary after the radiation boundary is applied.

3.3. Model Validation

The FVCOM for LPE has been well established with validations using observations made in several deployments throughout the years (between 2007 and 2016). More specifically, we deployed acoustic Doppler current profilers (ADCPs) and water pressure sensors for measurements of hurricane storm surges, water transport, and saltwater flux (Li et al., 2009, 2010) and for cold front-induced storm surges and water transport (Huang & Li, 2017). In Huang and Li (2017) skill assessment is done to show the reliability of the FVCOM's flow calculations at the inlets. An ADCP was deployed in the Rigolets at 30°10′15″N and 89°40′28″W. Another ADCP was deployed at Chef Menteur at 30°05′4″N and 89°47′29″W in 2008. The skill scores for the along channel velocity at these two stations are 0.82 and 0.87, respectively. In 2016, we deployed several water pressure sensors between 28 January and 24 March 2016 at east (30°9′19″N, 89°51′21″W), west (30°6′28″N, 90°25′20″W), north (30°21′23″N, 90°4′14″W), south (30°1′14″N, 90°9′31″W), and central (30°12′N, 90°7′21″W) stations as shown by the blue squares in Figure 2. The sampling was made at 30-min intervals. The skill scores for the water level simulations at these stations are 0.87, 0.78, 0.81, 0.84, and 0.84 for the east, west, north, south, and central stations, respectively (Figure 4). All of these are considered *excellent* for the model performance (Allen et al., 2007). The corresponding R^2 values are 0.79, 0.78, 0.67, 0.75, and 0.73 for the east, west, north, south, and central stations, respectively. These would be considered *very good* using R^2 values (Henriksen et al., 2003; Maréchal, 2004).

4. Model Results

4.1. Experiment 1: A Process Study and Flow Regime Analysis

For Experiment 1 (Table 1), the model is run with tidal input at the open boundary from 24 September through 1 December 2005. The observed wind is added after 8 November, and therefore, only 23 days of results from 8 November to 1 December are used here for the analysis. Wind during this time alternated between northerly and southerly. In the beginning (8 November), wind was relatively weak and mostly from the north. It then turned to southerly between 12 and 16 November, followed by about a week relatively strong northerly between the 16 and 28 November. A 2-day southerly, 1-day weak northerly, 2-day southerly, and then 2-day northerly followed in that order.

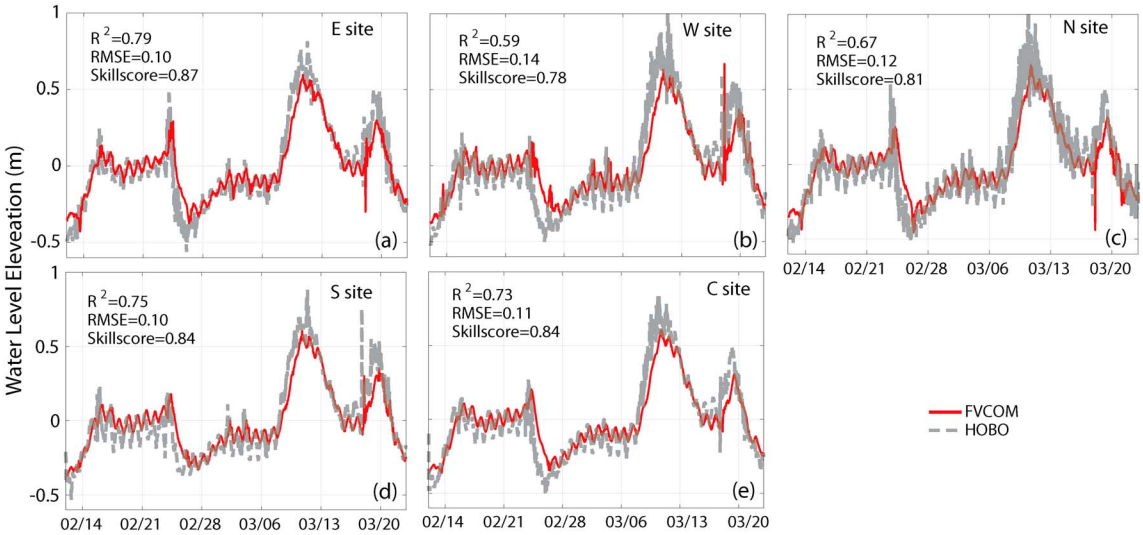

Figure 4. Comparison between Finite Volume Community Ocean Model (FVCOM) results and measurements from five HOBO pressure sensors. The R^2 values, root-mean-square errors (RMSEs), and skill scores for each site are shown. The comparison for the east, west, north, south, and central sites are shown in a, b, c, d, and e, respectively. Note that H1, H2, H3, H4, and H5 in Figure 2 shows the locations of HOBO pressure sensor deployments made in 2016 from 12 February to 24 March.

For convenience of analysis and discussion, within the model domain, we select 20 points in the LPE representing different areas for evaluation of the flow characteristics (Figure 3 and Table 2). These selected locations represent the eastern region (points 16, 17, 19, and 20 in Figures 5a and 5b), central region (points 4, 5, 11, 9, and 18 in Figures 5c and 5b), southern shores (points 1, 2, 3, 6, and 7 in Figures 6a and 6b), and western and southwestern coastal region (points 8, 14, and 15 in Figures 6c and 6d). The time series from the model results for each of the triangles nearest to each of the selected locations at 15-min intervals are used in the analysis.

Table 2
Lat/Lon and UTMs of Selected 20 Points

Point #	Longitude (W)	Latitude (N)	UTM_x (M)	UTM_y (M)	Vamp (cm/s; without wind)
1	−89.9962	30.0592	1,128,925.9	173,580.65	2.75
2	−90.0875	30.0484	1,120,136.2	172,284.37	10.93
3	−90.1633	30.0464	1,112,829.3	171,985.64	2.49
4	−90.0801	30.1072	1,120,778.5	178,809.49	3.43
5	−90.0621	30.1602	1,122,448	184,703.11	4.08
6	−90.1651	30.0309	1,112,673.2	170,265.87	3.71
7	−90.0868	30.0372	1,120,217.2	171,043.72	9.51
8	−90.2255	30.0919	1,106,782.6	176,969.26	2.3
9	−90.1865	30.1583	1,110,468	184,366.09	2.86
10	−90.1565	30.2391	1,113,265.7	193,351.45	3.03
11	−90.0352	30.2257	1,124,956.7	191,992.25	4.69
12	−90.225	30.2948	1,106,613.3	199,459.76	3.09
13	−90.2859	30.1874	1,100,864.2	187,499.94	2.43
14	−90.3226	30.1082	1,097,407.6	178,689.46	1.85
15	−90.4162	30.1585	1,088,342.7	184,188.99	7.31
16	−89.9634	30.1471	1,131,971.9	183,360.68	5.54
17	−89.9278	30.2073	1,135,319.4	190,074.75	8.26
18	−90.1143	30.3194	1,117,232.4	202,294.68	2.51
19	−89.8575	30.1835	1,142,121.2	187,521.87	16.39
20	−89.8105	30.1459	1,146,702.4	183,413.6	18.27

Note. UTM: Universal Transverse Mercator

The model results show that tide in LPE is generally very weak with a diurnal tidal range of less than 0.1 m for the most part, even though outside of LPE the tidal range is ~0.6 m (Forbes, 1988; Harris, 1981). Our model results are consistent with the study of, for example, Haralampides (2000), which shows a tidal range of 0.11 m inside LPE, Swenson and Chuang (1983), which separated the tidal and wind-driven transport by low-pass filtering. Indeed, the constriction of inlets have been found to alter tides inside a lagoon (e.g., Fernandes et al., 2004; Hill, 1994). Tidal currents are thus weak as well. As marked in Figure 3 at the 20 selected locations, tidal velocity amplitude is generally weak (approximately a few centimeters per second) except in the eastern bay (EB in Figure 2), for example, locations 19 and 20, where tidal velocity amplitudes are 16.39 and 18.27 cm/s (Figures 5a and 5b), respectively. The EB tidal currents have larger east component than north component (Figures 5a and 5b), indicating a stronger tidal oscillation along the longer axis of LPE. The progressive velocity vector diagram (Emery & Thomson, 2004) resembling the particle trajectories for the EB positions demonstrates that the water particles would mostly move in the east-west direction indicating tidal oscillation (Figure 7a). It should be noted that the progressive diagram is only used to show the general trend of the flow direction and should not be used as an accurate measure of transport (Carlson et al., 2010).

Based on our own vessel-based surveys using a boat-mounted ADCP, the tidal current velocity is indeed very small and difficult to measure on a moving vessel. The tidal current signal is pretty much buried in

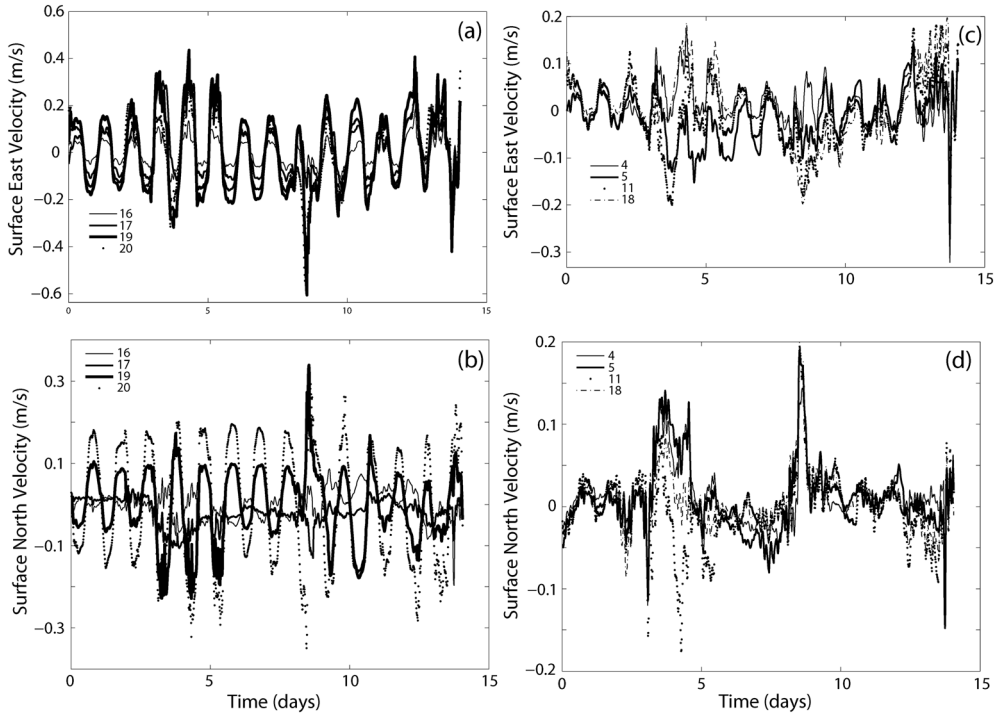

Figure 5. Model velocity time series at selected points in the eastern region: (a) the east component and (b) the north component. Model velocity time series at selected points in the central region: (c) the east component and (d) the north component. The numbers on the legend are numbers corresponding to the points selected (Figure 3).

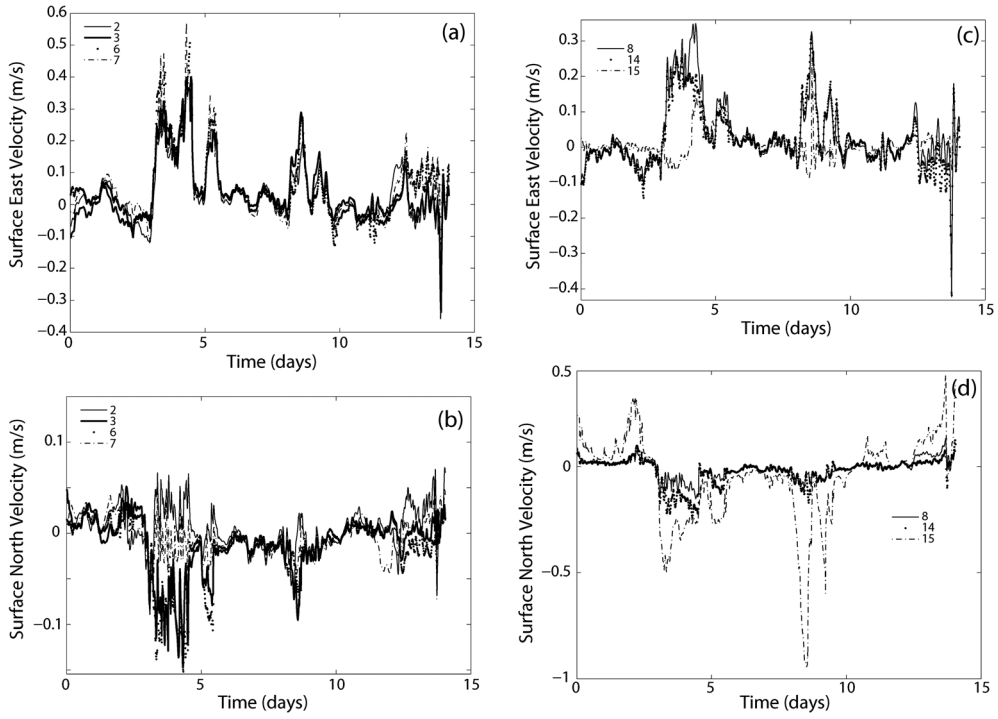

Figure 6. Same as Figure 5 but for the southern region: (a) the east component and (b) the north component. For the western region: (c) the east component and (d) the north component.

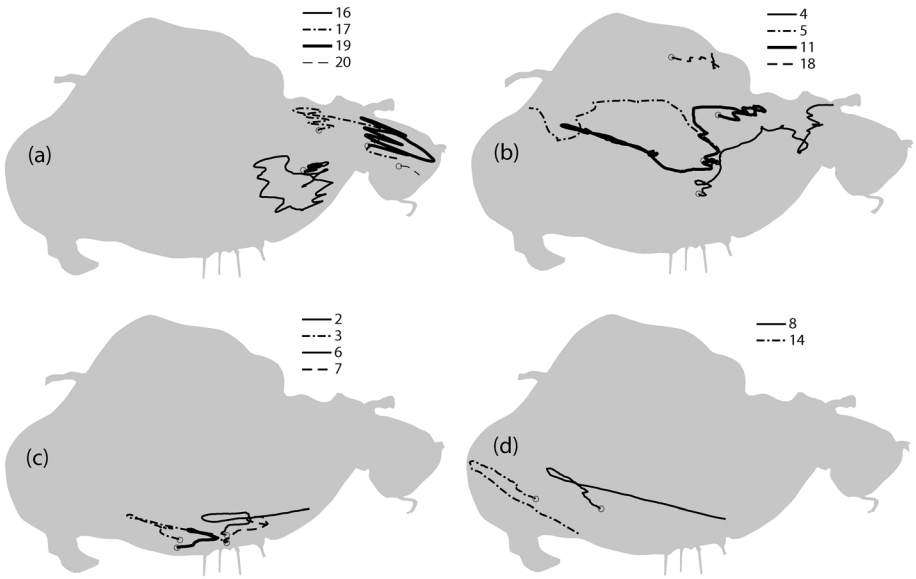

Figure 7. Progressive diagram plot of flows at given points. (a) Eastern region, (b) central region, (c) southern region, and (d) western region. The red dots show the start positions.

the noise. The observations were conducted early in October and November of 2005 during calm weather conditions.

The central basin, represented by locations 4, 5, 11, and 18 (Figures 5c and 5d), demonstrates weaker tidal currents, although the east velocity component still has a significant tidal signal (Figure 5c), the north velocity component (Figure 5d) is less tidal and more affected by the wind forcing. The magnitude of the velocity in both directions however is still relatively small, compared to that of the EB. The particle excursion is also mostly along the east-west direction, even though with some obvious north-south component (Figure 7b).

The southern coastal region, represented by locations 2, 3, 6, and 7 (Figures 6a and 6b), shows quite different flow characteristics. It has little tidal signal. The much stronger currents, compared to the central and eastern basins, appear to be a wind driven feature. This strong current is along the coastline mostly from the west to the east. Over 90% of the time the east velocity is positive (eastward), and even when the east velocity is negative, the magnitude is very small (Figure 6a). The north velocity component is much smaller (Figure 6b), an expected result as these locations is very close to the shore. Consequently, the particles move consistently along the coast toward the east (Figure 7c), with magnitudes 2–3 times of those in the eastern and central basins. The particle excursion rate reaches about 60 km in 15 days or 4 km/day.

The western coastal region, represented by locations 8, 14, and 15, has also very strong coastal currents (Figures 6c and 6d). The east velocity in this region can be very large (Figure 6c). The north velocity component is the largest within the entire basin: It reaches ~0.9 m/s at location 15 during a strong wind event (Figure 6d). As a result, the strong and almost unidirectional currents yield large particle excursions (Figure 7d) close to a rate of 90 km/15 days toward the south.

In summary, the eastern tidal regime, central wind-driven flow regime, and western and southern wind-driven coastal current regimes form the hydrodynamic system of the LPE. Since the eastern tidal regime has a small area, most of the estuary has very weak tidal currents. Wind provides the dominant force of water transport and dispersion. The wind effect is especially significant along the southern shore and western shore.

4.2. Experiments 2–4: Real-Case Simulation and Local and Remote Effects

Experiments 2–4 cover the period between 12 February and 24 March 2016. The computations with scenarios of local (Experiment 2), remote (Experiment 3), and combined local and remote winds (Experiment 4) allow us to show in this system that the remote wind effect (water level perturbation propagated through the open boundary) controls the overall water level variation inside the LPE, while the local wind stress causes the water level slope inside the system (Huang & Li, 2017). It is found that the low-pass-filtered water response

to local wind variation is very well approximated by a simple quasi steady state balance between the wind stress and the surface slope-induced pressure gradient in both east-west and north-south directions,

$$0 = -g\frac{\partial \zeta}{\partial x} + \frac{\tau_{ax}}{\rho h}, 0 = -g\frac{\partial \zeta}{\partial y} + \frac{\tau_{ay}}{\rho h}, \quad (11)$$

in which x, y, ζ, τ_{ax}, τ_{ay}, ρ, h, and g are the east and north distance (coordinate), water elevation from the mean sea level, wind stress in x and y, water density, and water depth at equilibrium when there is no force, respectively. In general, if the wind varies in magnitude and direction, the above balance would not hold and a local acceleration would have to be included. The 40-hr low-pass-filtered results show that the water level difference from the FVCOM results can be reproduced by (11) remarkably well. This is true for the simulation for 2005 period (Experiment 1), the simulation for the 2008 period (Huang & Li, 2017), and the simulation for the 2016 period (Figure 8). Figure 8a shows the comparison of water level differences from FVCOM and that from (11) for the local wind scenario calculated from values from the north and south stations (H1 and H2 in Figure 2). The R^2 value is 0.93 with a standard deviation of 0.01 m/s. Figure 8b shows the comparison of water level difference from FVCOM and that from (11) for the local wind scenario calculated from values from the east and west stations (H3 and H4 in Figure 2). The R^2 is a 0.76, with a standard deviation of 0.02 m. These indicate that in the north-south direction the balance of (11) is more accurate than that in the east-west direction, a fact that is likely due to the major opening of the system is the Rigolets in the east. In theory, equation (11) holds if the system is closed and has reached steady state. When there is an open boundary, flows through the open boundary will "relieve some pressure" and invalidate the balance given by (11).

Figure 8c shows the comparison of water level difference from FVCOM and that from (11) for the scenario with combined local and remote wind effects calculated from values from the north and south stations, while Figure 8d from the east and west stations. It can be seen that the results with combined effects in the north-south direction (Figure 8c) has a high R^2 value again (0.93) and is almost identical to that with the local wind (Figure 8a). This further verifies that the remote wind essentially does not contribute to the north-south direction water level difference. In the east-west direction (Figure 8d), this is a little different, the R^2 becomes smaller (0.48). It however still shows significant similarity between the two. The reason for the reduction seems to indicate that the open boundary water level variation contributes to some degree the surface slope in the east-west direction. We will discuss the mechanism of this quasi steady state balance in section 4.5 when we examine Experiment 7.

4.3. Experiment 5: Constant Winds

Because of the quasi steady state nature discussed above, the study of the wind-driven motion with constant wind forcing for different wind directions can provide useful information because the circulation under constant wind would be very similar to that when wind also has temporal variations. This, of course, is not to exclude the importance of temporal variation but rather a simplification of a complex problem. Figure 8 and the work of Huang and Li (2017) provide the rationale and confidence of this simplification. Based on these, the following wind-driven flow experiment is discussed.

For the numerical experiment, we use constant wind from eight different directions, that is, north, south, east, west, northeast, southwest, northwest, and southeast winds. For convenience, we use a wind speed of 5 m/s. The rationale of choosing the eight different wind directions can be argued by looking at the statistical wind regimes for different months. For that purpose, we use a 5-year record of wind for the area between the years 2011 and 2016 and produce wind rose diagrams for each month (Figure 9). It can be seen that January has mostly north-northwest winds; July has mostly southerly winds; October has mostly west-northwest winds; April has mostly southwesterly winds; and so forth. The following will discuss the model results for both surface and bottom flows grouped in pairs of winds of opposite directions.

4.3.1. Circulation Under North and South Winds

Under northerly wind (Figure 10a), the major surface current is along western shore and southern shore, extending offshore for about 10–15 km. This occurs in an area of mostly shallow water between 1 and 3 m except the central southern shore where the depth can be 4–5 m or more (Figure 2). The western shallow water has broad flows southward on surface. The majority of the southern shore has eastward flows, while the southeastern shore has southwestward flows, converging with the eastward flow near the Industrial

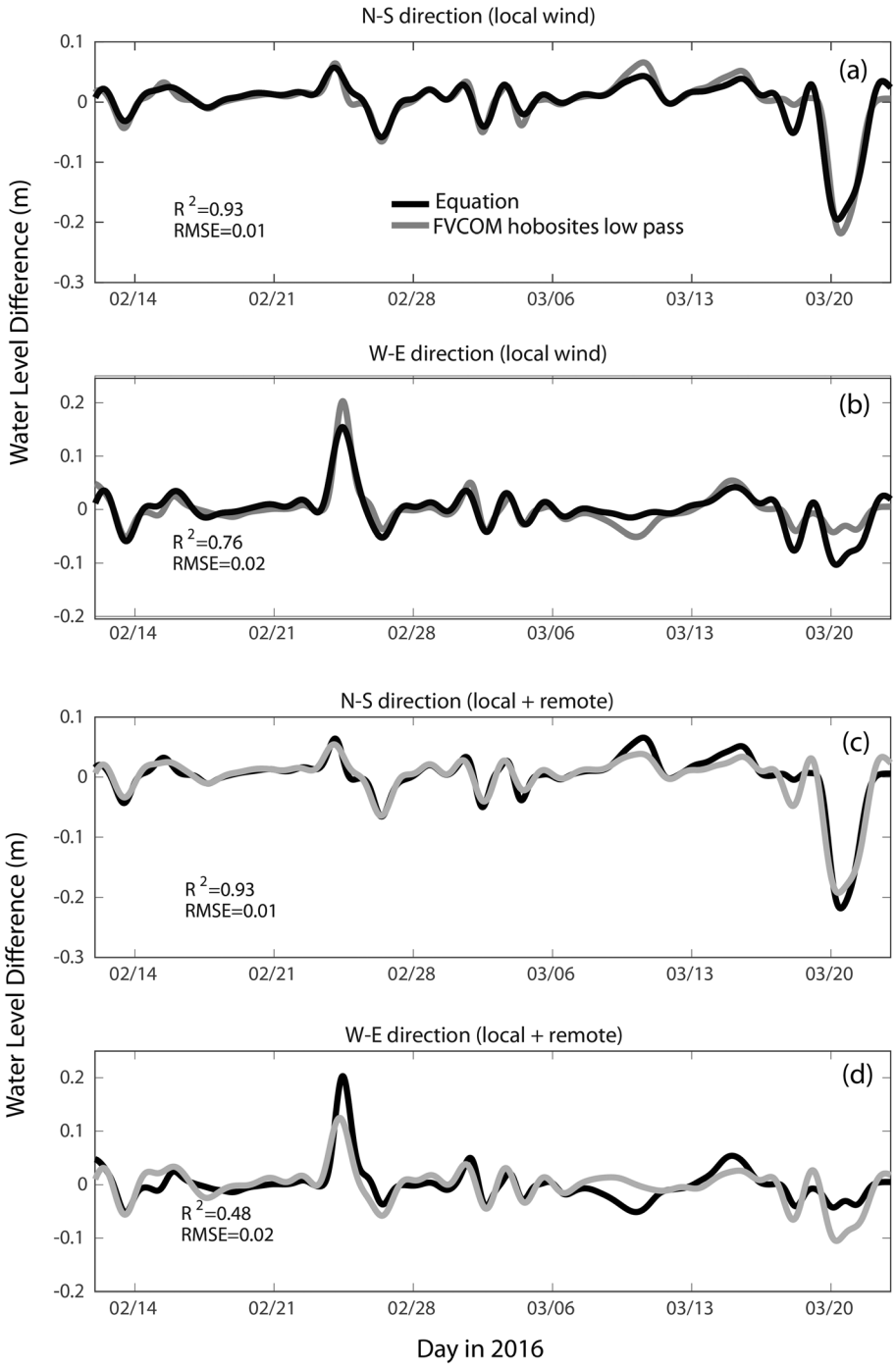

Figure 8. Comparison of low-pass-filtered water level difference (m) between Finite Volume Community Ocean Model (FVCOM) results and those from the linear steady state equation: water level difference between (a) the north and south (north minus south); (b) the east and west (east minus west) for local wind experiment; water level difference between (c) the north and south (north minus south); and (d) the east and west (east minus west) for local-remote wind experiment. Measured wind between 12 February and 24 March 2016 are used. RMSE = root-mean-square error.

Canal (denoted by IC, Figure 10a). The northern most point has a divergence, where the flow is very weak. The northeastern coast has southeastward flows. The eastern shore of the EB also has southward flow, with effects generated from the curvature of the coastline. The interior surface flow shows weak gyres (denoted by G). In the middle of LPE, we can see some crosswind surface flows, resembling what the

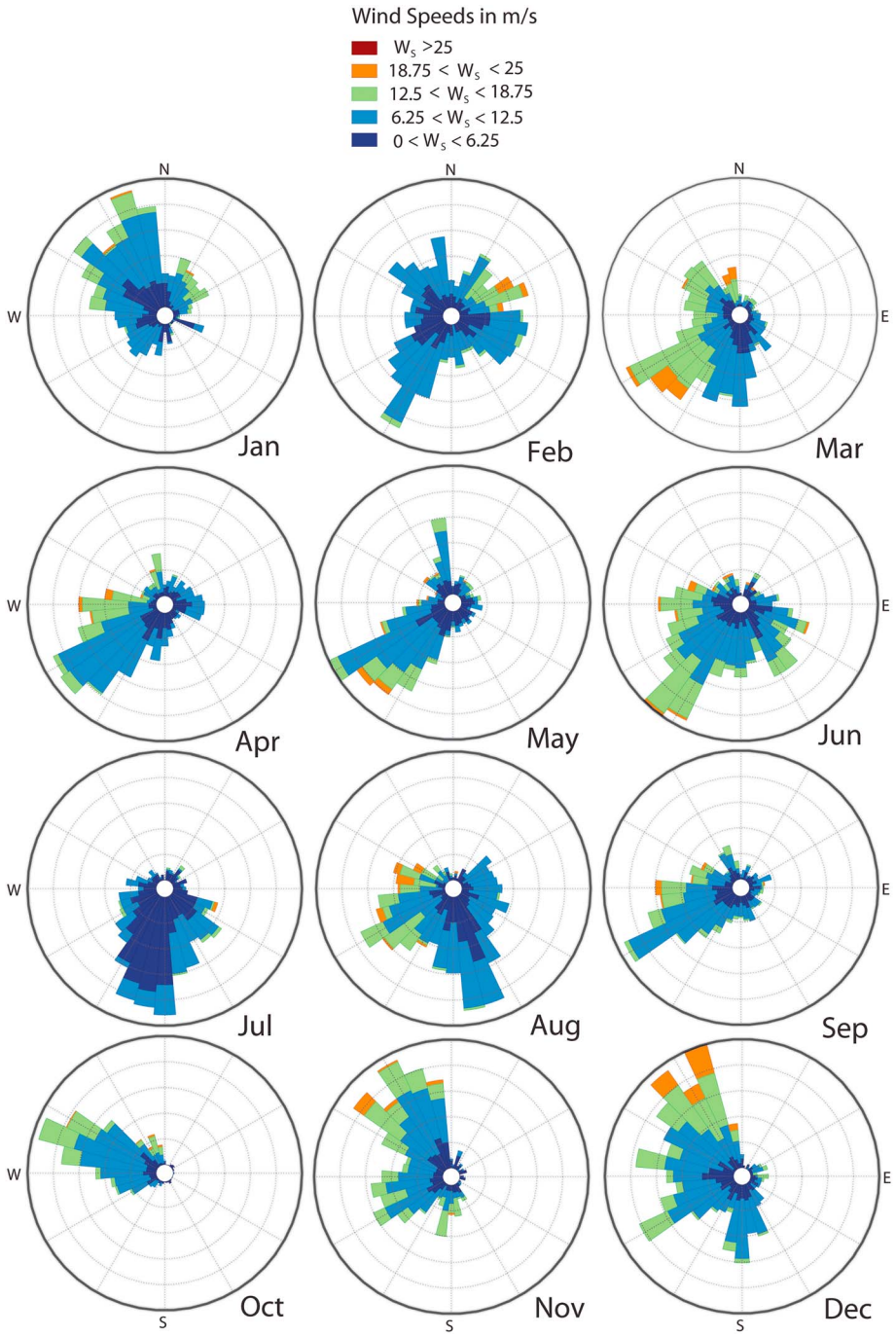

Figure 9. Wind rose plot for each month from 5-year data (2011–2016) from the study area.

Csanady (1968) model predicts, that is, ~90° to the right of the wind vector. The magnitude of the interior flow however is small compared to those boundary currents. If the wind reverses direction, that is, under southerly wind conditions (Figure 10b), the surface flows will roughly reverse directions with an otherwise similar pattern. The east of the Industrial Canal entrance area is now a surface flow divergence point, and the northern most point sees a convergence. The southernmost point in the EB is also a divergence point.

The bottom flows are however somewhat different. Under northerly wind (Figure 10c), the coastal currents along the western, southern, and eastern shores are very similar to that on surface but with a reduced magnitude. The reduction is by half or more. The interior flow is what sets the major difference from that on

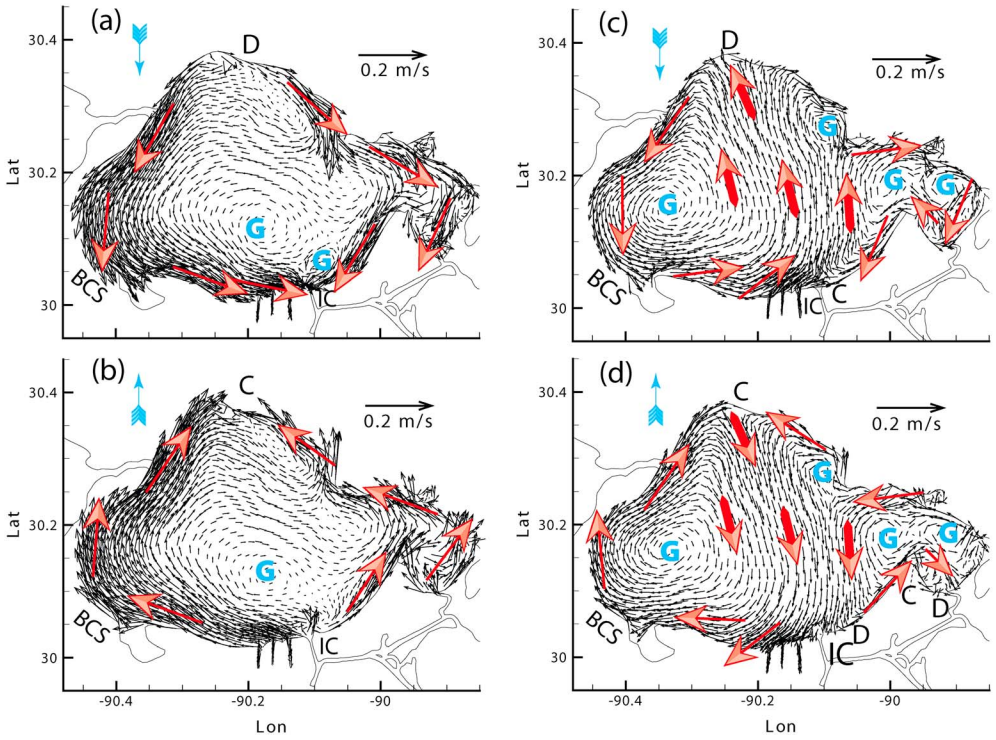

Figure 10. Flows from Finite Volume Community Ocean Model for (a) surface and (c) bottom under north wind. Flows from Finite Volume Community Ocean Model for (b) surface and (d) bottom under south wind. BCS stands for Bonnet Carré Spillway; G, C, and D indicate locations of gyre center, convergence, and divergence, respectively.

surface. The central interior is seen to have a ~30-km-wide northerly flows that are against the wind. The magnitude is now comparable to those of the coastal currents. This makes the flow field to be much more uniform within the entire LPE. Several gyres are seen to form for transition to the coastal currents from the interior counter-wind flows. These gyres are different in locations as those on surface. In general, there is significant vertical shear of velocity as the bottom flows on the coast are weaker than those on surface, while the interior flows are much stronger than those on surface. The locations of flow divergence and convergence are roughly the same as on surface. When the wind reverses its direction, that is, under southerly wind (Figure 10d), the coastal currents all reverse directions and the interior flows also change directions to against the wind. The gyres remain at the same locations and with about the same size but with reversed circulations.

4.3.2. Circulation Under East and West Winds

For easterly wind, the surface currents are westward (Figure 11a) and strong on the northern and southern shores. The surface currents on the southern shore are much narrower than those on the northern shore. The former is about a couple of kilometers wide, while the latter about 10–15 km wide. This is apparently due to the broad shallow water along the northern shore. These surface coastal currents converge at about the western most point of the LPE. A weak return flow on the surface can be seen at the west end, forming to its south a gyre northeast of the Bonnet Carré Spillway. In contrast, a point of divergence is seen at the easternmost point (Figure 11a). The interior flow in this case is also very weak and even less defined in terms of pattern. It changes direction from east to west along the central interior of the lake. For example, in the eastern portion between 90.15° and 90 W longitudes, the interior surface flow is cross the wind to the right, similar to Csanady (1968, 1982). In the western portion between 90.2° and 90.35 W longitudes, the surface currents reverse directions but even weaker than the east. This is contrary to the Csanady model. When the wind reverses direction to a constant westerly wind (Figure 11b), again, the coastal currents reverse directions. The western most point now has a divergence of flows, forming a similar gyre but with opposite circulation northwest of the Bonnet Carré Spillway. The divergence point is more like a stagnant point as the flow magnitude is very small. The surface flows converge at the east point.

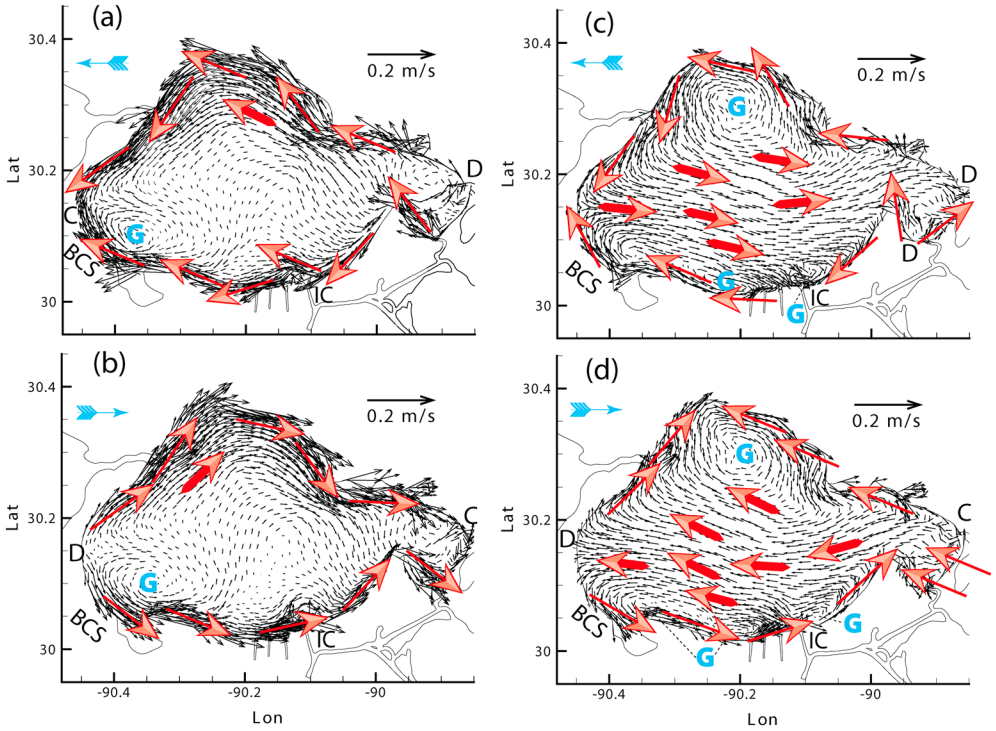

Figure 11. Flows from Finite Volume Community Ocean Model for (a) surface and (c) bottom under east wind. Flows from Finite Volume Community Ocean Model for (b) surface and (d) bottom under west wind. BCS stands for Bonnet Carré Spillway; G, C, and D indicate locations of gyre center, convergence, and divergence, respectively.

For the easterly wind case (Figure 11c), the bottom coastal currents along northern, southern, western, and eastern shores are very similar to that on surface but with a reduced magnitude. The interior flow is different from that on surface. The central interior also has a wide and uniform easterly flow against the wind. Some gyres exist but different in locations as those on surface. Again, there is significant vertical shear of velocity. When the wind reverses its direction, that is, to a westerly wind (Figure 11d), the coastal currents all reverse directions and the interior flows also change directions to against the wind. The gyres remain at the same locations and with about the same size but with reversed circulations.

4.3.3. Circulations Under Northeast, Southwest, Northwest, and Southeast Winds

The surface circulation patterns under northeasterly, southwesterly, northwesterly, and southeasterly winds are shown in Figures 12a, 12b, 13a, and 13b, respectively. The bottom circulation patterns under northeasterly, southwesterly, northwesterly, and southeasterly winds are shown in Figures 12c, 12d, 13c, and 13d, respectively. Though the details vary, the common characteristics are still the same: Shallow waters tend to have downwind flows, while deep waters tend to have upwind flows. The bottom has return flows in the interior that are relatively strong and broad; while along the coastlines it has coastal current guided by the wind and orientation of the coast.

4.3.4. Vertical Structure of Coastal Currents

It is shown in the above discussion that in Lake Pontchartrain wind generates strong coastal currents and the bottom return flow is broad and relatively strong compared to the surface flows. To have a better view of the vertical structure of the wind-driven coastal currents, we select four transects perpendicular to the coastline (the dashed lines marked as 1, 2, 3, and 4 in Figure 2) and extracted the flow profiles (Figure 14) from the model results for the various wind-driven flows after reaching equilibrium (steady state). It can be seen that the coastal currents under various wind conditions can be a few kilometers to more than 10 km wide. It is mostly from surface to bottom at the coast (Figures 14a–14p) and becomes two layers offshore (typical examples—Figures 14a, 14c, 14e, and 14g). These four transects also cover some of the interior flows. Away from the coastal currents, the interior can be seen having return flows against the wind. The most remarkable examples are shown in Figures 14d and 14h. These features are not present in the Csanady (1968, 1982) model but can be explained by the Engelund (1973) model.

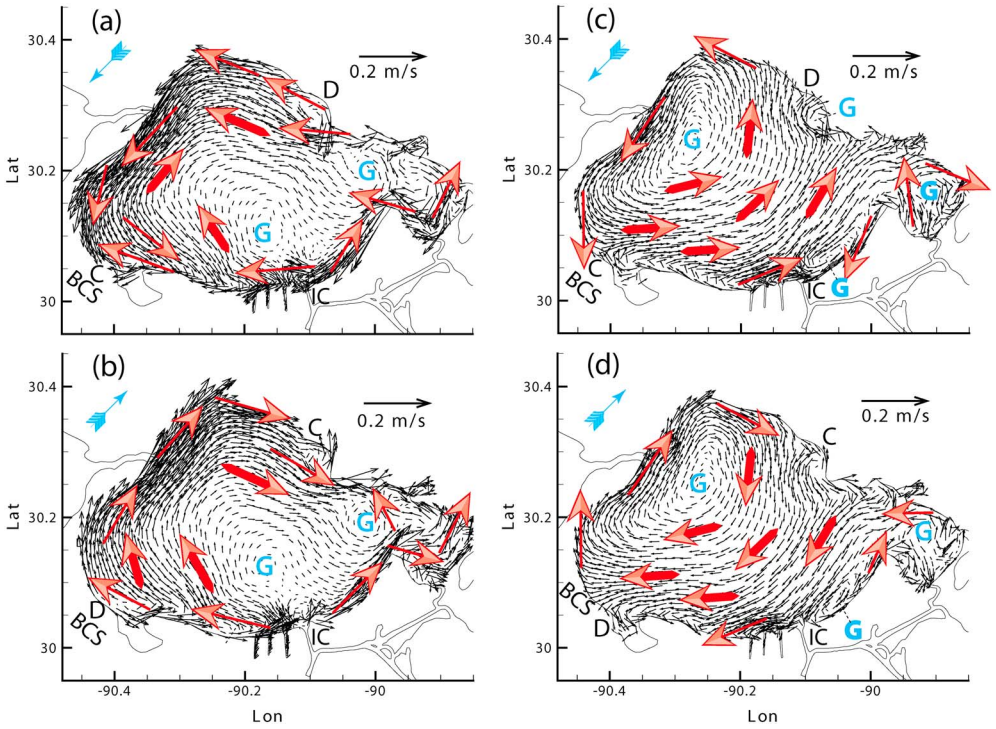

Figure 12. Flows from Finite Volume Community Ocean Model for (a) surface and (c) bottom under northeast wind. Flows from Finite Volume Community Ocean Model for (b) surface and (d) bottom under southwest wind. BCS stands for Bonnet Carré Spillway; G, C, and D indicate locations of gyre center, convergence, and divergence, respectively.

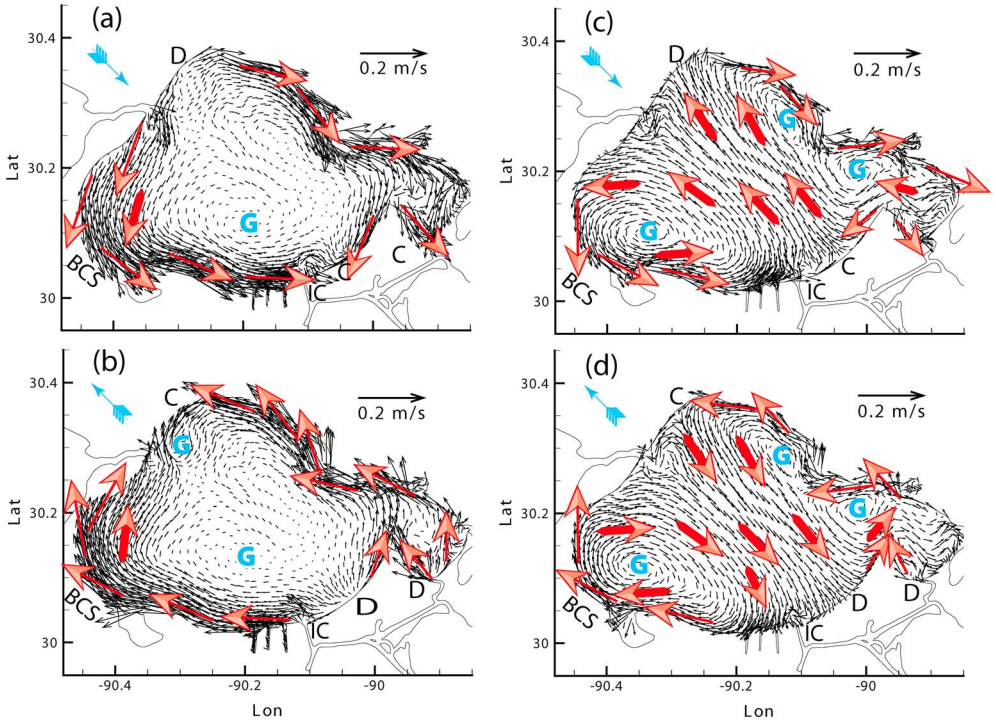

Figure 13. Flows from Finite Volume Community Ocean Model for (a) surface and (c) bottom under northwest wind. Flows from Finite Volume Community Ocean Model for (b) surface and (d) bottom under southeast wind. BCS stands for Bonnet Carré Spillway; G, C, and D indicate locations of gyre center, convergence, and divergence, respectively.

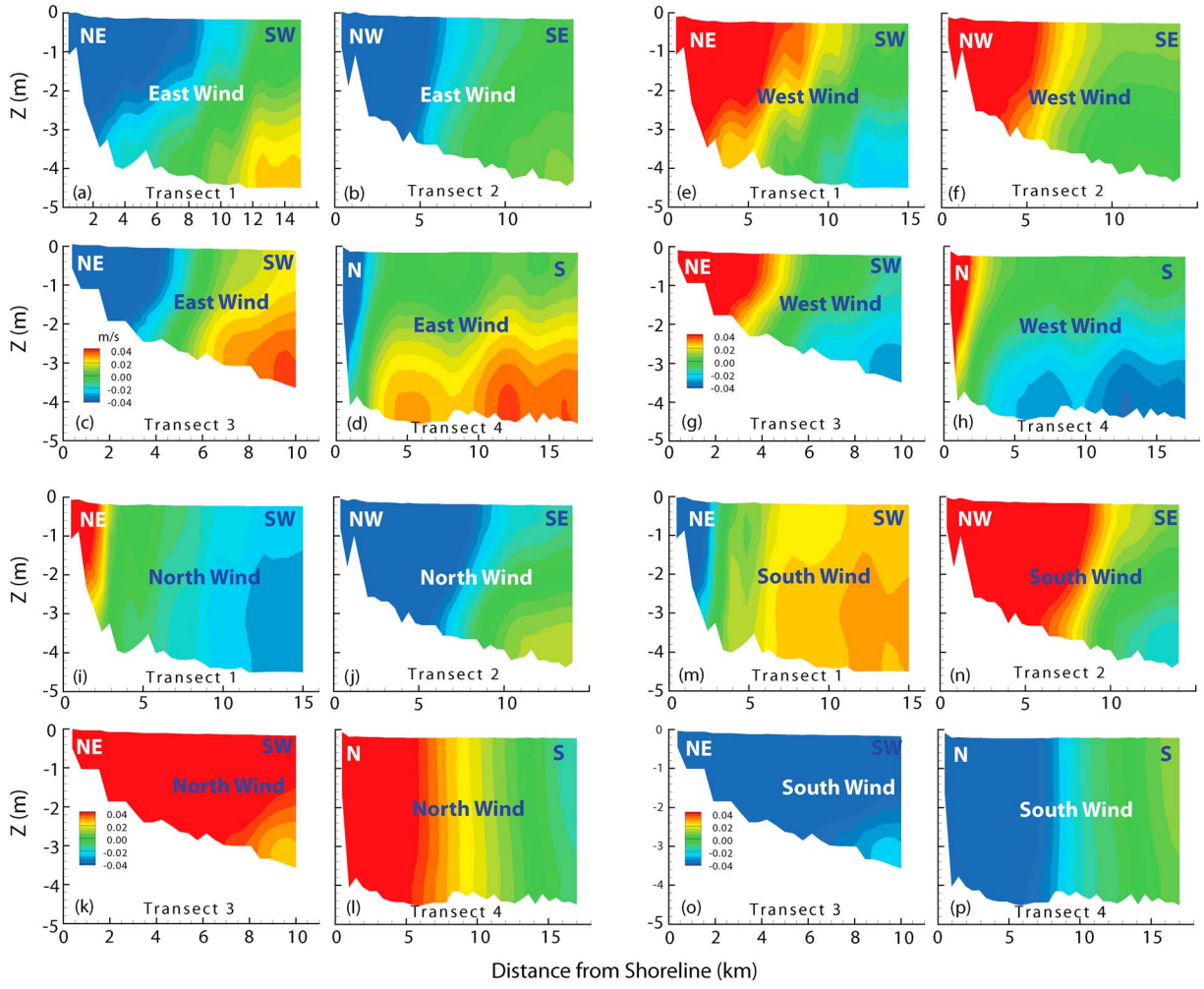

Figure 14. Along shore current profiles along the four selected transects (as marked in Figure 2) from Finite Volume Community Ocean Model experiments. Results for the east, west, north, and south winds are shown in (a)–(d), (e)–(h), (i)–(l), and (m)–(p), respectively.

4.4. Experiment 6: Constant Wind Without Rotation

Experiment 5 suggests that regardless of wind directions, the coastal shallow water has strong downwind current in shallow water (often along the shoreline, forming coastal currents). Obviously, the coastal currents follow the wind and are guided by the coastline orientation. The majority bottom flows are against the wind. There is no consistent pattern in the interior that fits the theory of Csanady (1968, 1982).

In order to quantify the effect of Earth rotation in such a system, we conducted Experiment 6, with everything identical to Experiment 5, except that here we excluded Coriolis force. The results show clearly that the wind-driven flows under both conditions are almost identical. We have calculated the velocity difference from the two sets of model results using the following equation:

$$\alpha = \sqrt{\frac{\sum_{i=1}^{N}\left[(u_{1i}-u_{0i})^2+(v_{1i}-v_{0i})^2\right]}{\sum_{i=1}^{N}\left[{u_{1i}}^2+{v_{1i}}^2\right]}}, \tag{12}$$

in which i is the ith point for velocity, N is the total number of velocity points inside LPE, (u_{1i}, v_{1i}) are the east and north velocity components for results with Earth rotation at the ith point, and (u_{0i}, v_{0i}) are the east and north velocity components for results without the Earth rotation at the ith point. If the two are identical, this nondimensional parameter α value would be 0. This is similar to the stress value of Allen et al. (2007), in which a stress value <0.05 indicates an excellent consistency.

In our case, the α value from equation (12) is only 0.0034. Obviously, this demonstrates that ignoring Coriolis force in this problem does not affect the results. The system is too small for the effect of Earth rotation to be important. At the same time, the shallow water system makes a frictionless model irrelevant, and bottom friction becomes much more important than rotation. Once again, the frictional Engelund model without Earth rotation is more relevant for this type of wind-driven circulation.

4.5. Experiment 7: Dynamics of the Adjustment Process

We have seen remarkable quasi steady state balance between the wind and surface slopes, even when the wind is changing with time (Experiments 2–4). The steady state balance has been shown in Huang and Li (2017) in the LPE system and further confirmed here with more simulations and analysis. These give us a justification of conducting Experiments 5–6, which only include constant wind from fixed directions. These latter two experiments provide a comprehensive scenario of three-dimensional flow structures under different wind conditions. The coastal currents and wind-driven flow patterns are subsequently analyzed. Since the transient or adjustment process is short, these are useful in describing and interpreting subtidal (low frequency) circulations.

However, these experiments do not provide a mechanism for the quasi steady state balance. Here the Experiment 7 is conducted, aiming at the explanation of fundamental mechanism of the balance in such a system with a closer look at the adjustment process (Gill, 1982). Figure 15 shows the result of this experiment. For convenience and brevity, we show the surface slope time series in the north-south (Figure 15a), and east-west (Figure 15b) directions, respectively. It is obvious that the surface slopes in both directions can quickly adjust to the new equilibrium when the wind has a sudden change in direction. This is shown by the spikes of slopes after each variation in wind direction and subsequent quick return to the new equilibrium. When these short-term variations are zoomed in, they appear as forced damped oscillations (Figures 15c and 15d; Tenenbaum & Pollard, 1985). Since the governing physics of the present problem is a shallow water motion with friction, hydrostatic gravity waves can be generated by an atmospheric perturbation. The forced damped oscillations should be similar to the solution of the following equation (Appendix A):

$$m\frac{\mathrm{d}^2y}{\mathrm{d}t^2}+2mr\frac{\mathrm{d}y}{\mathrm{d}t}+m\omega_0 y=f(t), \tag{13}$$

in which m, r, and ω_0, are all constants; t is time; y is the dependent variable (here the water slope); and $f(t)$ is the forcing function. The solution would be a forced damped oscillation in a form like (Tenenbaum & Pollard, 1985)

$$y=ce^{-rt}\sin\left(\sqrt{\omega_0^2-r^2}t+\delta\right)+G(t), \tag{14}$$

in which the first term on the right-hand side is a free damped function and the second term G is another damped motion approaching to a constant. In mathematics, G is a convolution (Boas, 2006) between the wind stress and the surface slope. The G function contains various frequencies, but only the one that matches the natural oscillation frequency of the system will be significant. The natural oscillation frequency of the LPE in the north-south direction is different from that in the east-west direction as the wave propagation period differs due to the length difference. The fundamental seiche period (Proudman, 1953; deBoer & Maas, 2011) of the system is defined by

$$T=\frac{2L}{\sqrt{gh}}, \tag{15}$$

in which T, L, g, and h are the period of seiche oscillation, the distance between two reflection points on opposite coasts, gravitational acceleration, and mean water depth, respectively. Since the north-south distance between stations H1 and H2 is L = 35 km, and east-west distances between stations H3 and H4 is L = 52 km (Figure 2), equation (15) gives the seiche periods in these directions as 3.1 and 4.6 hr, respectively. Figures 14c and 14d show that these are very accurate approximations. In addition, the seiche oscillations are damped in two to three cycles, a time much shorter than the 40-hr low-pass filter period. This makes the subtidal response to wind change almost *instantaneous* or quasi steady state. This is in contrast to long systems,

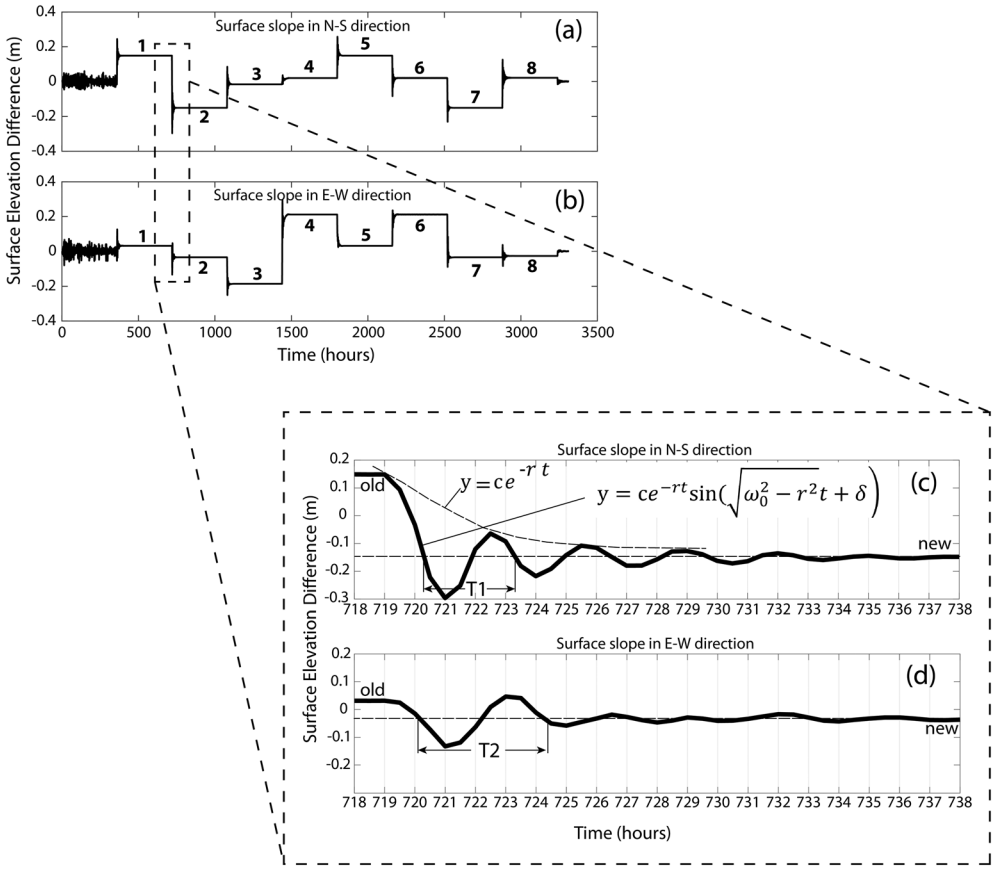

Figure 15. Adjustment experiment. Time series of surface difference from Finite Volume Community Ocean Model numerical experiment with step changing wind. Wind is constant for each step. The simulation is continuous. (a) Time series of surface difference between north and south. (b) Time series of surface difference between east and west. (c) Zoomed-in view of time series of surface difference between north and south for seiche. (d) Zoomed-in view of time series of surface difference between east and west for seiche. The numbers 1 to 8 in (a) and in (b) indicate the south, north, east, west, south, west, north, and southeast winds, respectively. T1 ~ 3.1 hr and T2 ~ 4.6 hr, consistent with seiche oscillations.

which may have a seiche period of more than a day (e.g., Weaver, Johnson et al., 2016) in which quasi steady state may not apply unless the perturbation is dissipated in a short distance and so that no seiche is established.

5. Discussion and Conclusions

In this paper, we discuss seven numerical model experiments for LPE using FVCOM. These experiments confirm that LPE has a relatively strong tidal flow region in the EB and eastern interior. From this region, tidal velocity magnitude decreases westward and southward. The interior of the lake, however, is not significantly affected by tidal currents, but instead, by wind, showing strong variations without a clear tidal signal. These results however are specific to this system. The more important results are discussed and summarized below.

Along the coastlines, broad coastal current zones are shown, which are determined by winds. Return flows develop at the bottom. The most significant feature that deserves attention and cannot be overemphasized is that the quasi steady state balance is quite persistent in this system. The balance is between low-pass-filtered local wind stress force and low-pass-filtered surface slope pressure gradient force. The statistical consistency measure, that is, R^2 between the fully nonlinear three-dimensional FVCOM results and that from the linear steady state balance, equation (11), reaches a value as high as 0.93. This means that the low-pass-filtered wind-driven circulation in such a system has a quick adjustment to equilibrium almost at every change of the wind force.

Such a response to wind is not a case only applicable to the Lake Pontchartrain system. The wind-driven circulation in other similar system can have similar features (Lin et al., 2016). The commonality of this kind of system includes that (1) it is broad and shallow (low aspect ratio: depth/width or $h/W \sim 10^{-4}$ to 10^{-5}) and (2) it is relatively narrow at its opening (open boundary much shorter than the total perimeter of the system). It has been shown by numerical models for winter cold front-induced circulations in the Calcasieu Lake of southwestern Louisiana near Texas border (Lin et al., 2016) that wind-driven circulation produces downwind flows along the shallow coastal waters and return flow in the deep navigational channel. The wind-driven water level response follows the wind very closely (Feng & Li, 2010) in three Louisiana Bays—the Atchafalaya Bay, Timbalier Bay, and Barataria Bay. The aspect ratio for the Lake Pontchartrain is $h/W \sim 4/66{,}000 \sim 6 \times 10^{-5}$; for Calcasieu Lake, it is ~$2/30{,}000 \sim 6.7 \times 10^{-5}$; for Barataria, Atchafalaya, and Timbalier Bays, it is $2/40{,}000 \sim 5 \times 10^{-5}$. It appears that these shallow lagoons and bays respond to wind events in the same way as discussed here. The wind-driven circulation in such systems should be very much similar in character. These shallow and broad systems allow strong and fast dissipation of wind-induced perturbations so seiche will dissipate quickly (compared to tidal cycle).

Because of the quasi steady state nature of the wind-driven flows, the circulation patterns under constant winds from different directions can cover possible circulation patterns even the wind may be changing over time. We have provided the possible 3-D circulations with winds from eight different directions and discussed the downwind coastal currents, gyres, the broad and uniform bottom return flows, and the three-dimensional circulation structures across the shorelines. We also find that the effect of Earth rotation is negligible. Thus, it proves that the Csanady model is not applicable to this system.

We have explained the quasi steady state by a study on the adjustment process. We find that the adjustment process between steady state balances is a natural oscillation or seiche resulted from the change of wind. The time it takes for the seiche propagation between the northern and southern shores is about 3 hr, while that between eastern and western shores is more than 4 hr, which are all reproduced accurately by the model. It takes the seiche to oscillate only 2–3 times before almost completely dissipated. This results to a time period much shorter than the diurnal tidal cycle, and therefore, these oscillations can be significantly filtered out by a 40-hr low-pass filter. Therefore, the subtidal wind stress and subtidal surface slope pressure gradient force are in quasi steady state balance.

Appendix A: Derivation of the Forced Damped Oscillation Equation

Equation (13) is a typical forced damped oscillation equation. Here we provide an example to relate this equation to the problem that we are discussing, that is, the shallow water wind-driven motion. For simplicity, we will start from the following linear equations in a one-dimensional channel with a constant undisturbed water depth.

$$\frac{\partial u}{\partial t} = -g\frac{\partial \zeta}{\partial x} + \frac{\tau_{ax}}{\rho h} - \frac{\beta u}{h}, \tag{A1}$$

$$\frac{\partial \zeta}{\partial t} + h\frac{\partial u}{\partial x} = 0, \tag{A2}$$

in which u, ζ, g, h, x, t, ρ, β, and τ_{ax} are the velocity, surface elevation, gravitational acceleration, depth, x coordinate, time, water density, bottom friction coefficient, and surface wind stress, respectively. The linear bottom friction coefficient β is related to the drag coefficient by (Li & Valle-Levinson, 1999; Parker, 1984; Proudman, 1953)

$$\beta = \frac{8C_d U_0}{3\pi}. \tag{A3}$$

The first equation is the barotropic depth-averaged momentum equation and the second the continuity equation. The discussion can be extended to two dimensions and with Coriolis effect involved. That will however significantly complicate the derivation and discussion. For the present wind-driven problem, the shallow water equations without Coriolis in one dimension is sufficient. For a problem with a change in wind stress, we can assume that the wind stress is a step function:

$$\tau_{ax} = \begin{cases} \tau(x)\tau_1, & (t < 0) \\ \tau(x)\tau_2, & (t >= 0) \end{cases} \tag{A4}$$

in which both $\tau_1$and τ_1 are constants, and $\tau(x)$ is a normalized (dimensionless) differentiable spatial function, representing the variation with x of the wind stress. For more general problems, the wind stress does not have to have a finite jump, that is, it can be a continuous function of time. We now do derivative to the first equation with respect to t and do derivative to the second equation with respect to x, yielding the following two equations:

$$\frac{\partial^2 u}{\partial t^2} = -g\frac{\partial^2 \zeta}{\partial t \partial x} + \frac{\tau(x)}{\rho h}\delta_\tau(t) - \frac{\beta}{h}\frac{\partial u}{\partial t}, \tag{A5}$$

$$\frac{\partial^2 \zeta}{\partial t \partial x} + h\frac{\partial^2 u}{\partial x^2} = 0. \tag{A6}$$

In equation (A5), the function $\delta_\tau(t)$ is a so-called delta function, which satisfies the following relationships:

$$\delta_\tau(t) = \begin{cases} \infty & (t = 0), \\ 0 & (t \neq 0), \end{cases} \tag{A7}$$

and

$$\int_{t_1}^{t_2} \delta_\tau(t')\,\varphi(t')\mathrm{d}t' = \begin{cases} (\tau_2 - \tau_1)\varphi(0), & (0 \in [t_1, t_2]), \\ 0, & (\text{otherwise}), \end{cases} \tag{A8}$$

in which $\varphi(t')$ is any continuous function of t. Eliminating ζ by substituting (A6) to (A5), we can obtain

$$\frac{\partial^2 u}{\partial t^2} = gh\frac{\partial^2 u}{\partial x^2} + \frac{\tau(x)}{\rho h}\delta_\tau(t) - \frac{\beta}{h}\frac{\partial u}{\partial t}. \tag{A9}$$

If wind stress is a continuous function of time, that is, no finite jump, the delta function will be replaced by a function related to the temporal derivative of τ_{ax}. The equation for water elevation ζ is similar (omitted here for brevity). Since this equation is linear, we can only examine one component from the Fourier expansion of the spatial function (i.e., in x) for u. In other words, we are looking for a solution with a factor of e^{ikx}, where $i = \sqrt{-1}$, and k is the wave number. This leads the derivative with respect to x to be equivalent to multiplying a factor of ik. For the second-order derive to x, this leads to a multiplication of $(ik)^2 = -k^2$. This leads to

$$\frac{\mathrm{d}^2\tilde{u}}{\mathrm{d}t^2} + \frac{\beta}{h}\frac{\mathrm{d}\tilde{u}}{\mathrm{d}t} + ghk^2\tilde{u} = \frac{\tilde{\tau}}{\rho h}\delta_\tau(t), \tag{A10}$$

in which all the variables with a tilde is for the Fourier coefficients at given wave number k. This is essentially the same format of (13) in the main text. Here the linear bottom friction is related to the damping coefficient of (13) by

$$r = \frac{\beta}{2h}. \tag{A11}$$

Appendix B: Discussion on Open Boundary Conditions

FVCOM has an option of five different radiation boundary conditions: (1) active sea level (ASL) condition, (2) clamped (ASL-CLP; Beardsley & Haidvogel, 1981), (3) Implicit Gravity Wave radiation (Chapman, 1985), (4) partial clamped gravity wave radiation (BKI; Blumberg & Kantha, 1985), and (5) explicit Orlanski radiation (ORE; Chapman, 1985; Orlanski, 1976). In our experiments, we selected ASL, that is, by specifying the water level and allowing the use of model to calculate the velocity. It has been recognized that there is still artificial or numerical effect when using this open boundary condition. Open boundary condition treatment is always an important issue for numerical experiments. A properly posed open boundary condition allows perturbations inside the domain to pass through the boundary without significant distortion

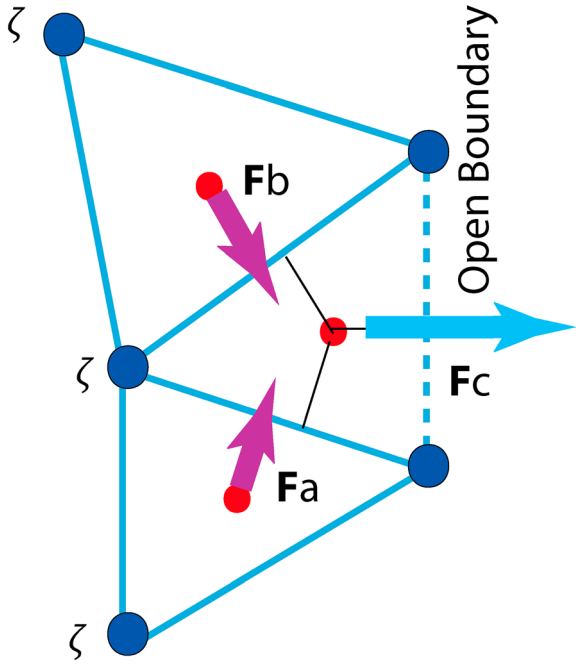

Figure B1. Open boundary treatment in Finite Volume Community Ocean Model.

to the interior solution (Orlanski, 1976). For problems with an open boundary being far away from the point of interest, a clamped condition can be used (Beardsley & Haidvogel, 1981). A clamped condition has also been used for storm surge computations without consideration of tides. Another method is the Sommerfeld radiation condition (e.g., Orlanski, 1976; Palma & Matano, 2001; Raymond & Kuo, 1984; Sommerfeld & Straus, 1967) that allows properties to *radiate* out of the region like a linear and inviscid wave only applied at the open boundary:

$$\phi_t + c\phi_x = 0, \tag{B1}$$

in which ϕ is a physical quantity and c a phase speed. A modified Sommerfeld radiation condition is given by Blumberg and Kantha (1985)

$$\phi_t + c\phi_x = -\frac{\phi - \phi_k}{T}. \tag{B2}$$

The additional term on the right represents a damping effect to force ϕ to certain value ϕ_k with a time scale of T. The condition used by Flather (1988) with an extensive open boundary (more than half of the perimeter of the region of interest in open boundary), a gravity wave radiation is provided in which both currents and elevation were imposed. In our model, the open boundary condition is similar to Flather (1988) but not the same. It uses a mass conservation requirement,

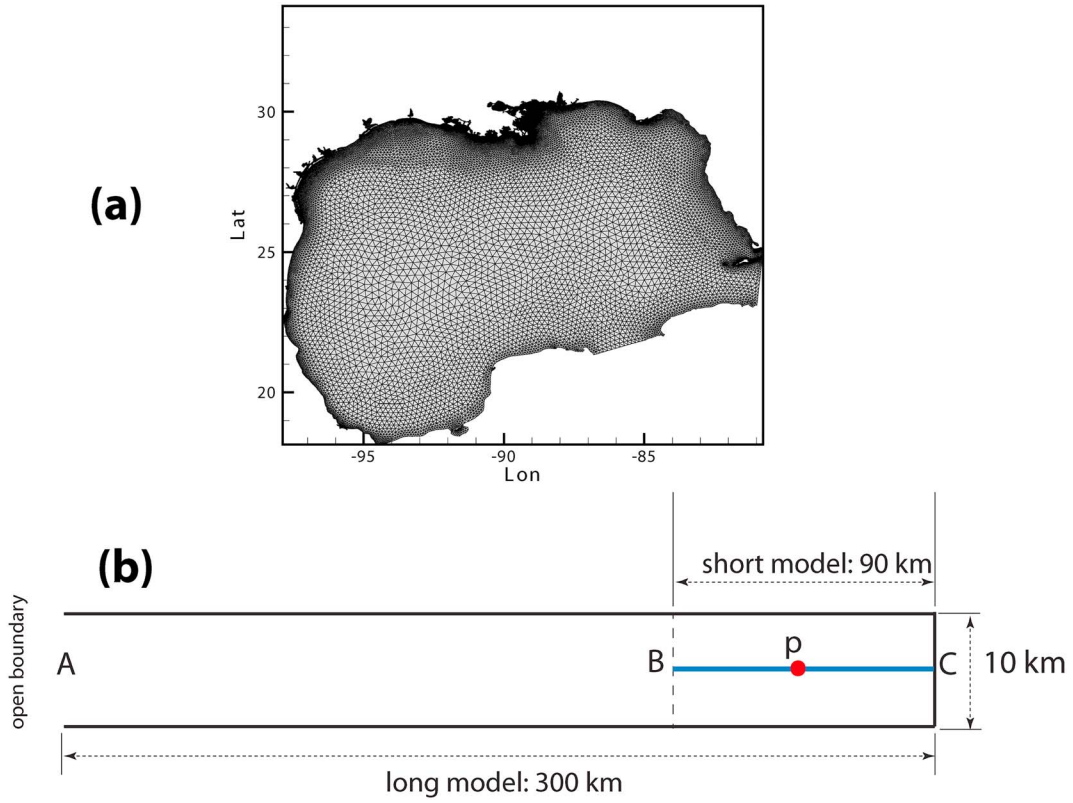

Figure B2. (a) A larger Gulf of Mexico model. It covers the entire domain of the original model for Lake Pontchartrain. The larger model mesh has 214,297 triangles and 119,566 nodes. (b) Idealized model domains for long and short models. The length of the longer model is 300 km (line AC), while the shorter model has a length of 90 km (line BC).

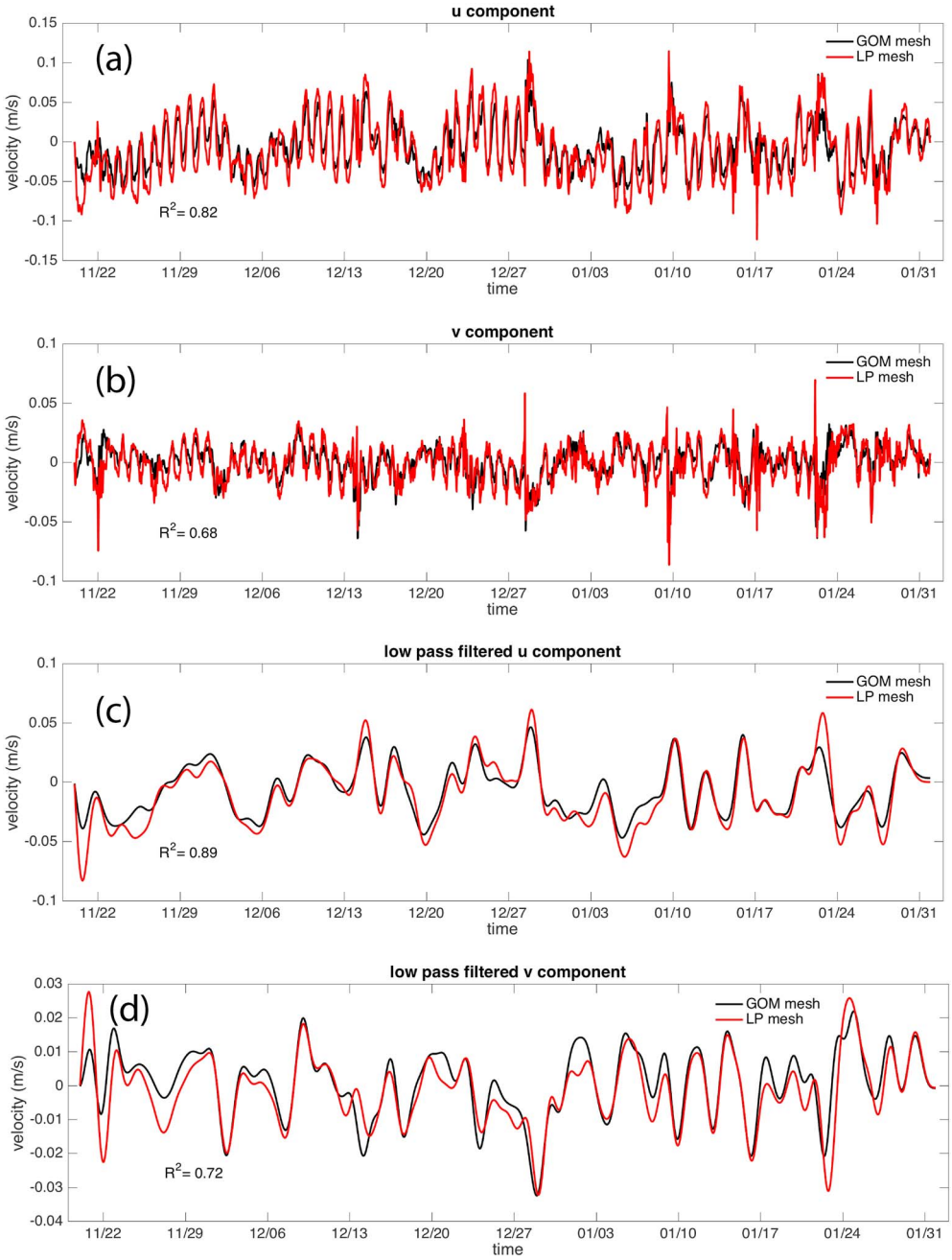

Figure B3. (a) Comparison of model results for east velocity component u from the Rigolets. The red color line is from the original smaller model, while the black line is from the larger domain model that does not have the open boundary at the study area. (b) Same as (a) but for the north velocity component *v*. (c) Same as (a) except that here we show the low-pass-filtered results for *u*. (d) Same as (c) but for *v*. GOM = Gulf of Mexico; LP = Lake Pontchartrain.

$$F_C = \frac{\partial \zeta}{\partial t} A - (F_A - F_B). \tag{B3}$$

As shown in Figure B1, F_A and F_B are the flux through the two sides of a boundary triangle, while F_C is the flux through the open boundary (perpendicular to the boundary). However, this open boundary condition may still cause numerical problems, and FVCOM allows the implementation of a sponge layer to dissipate any numerical reflection from the boundary.

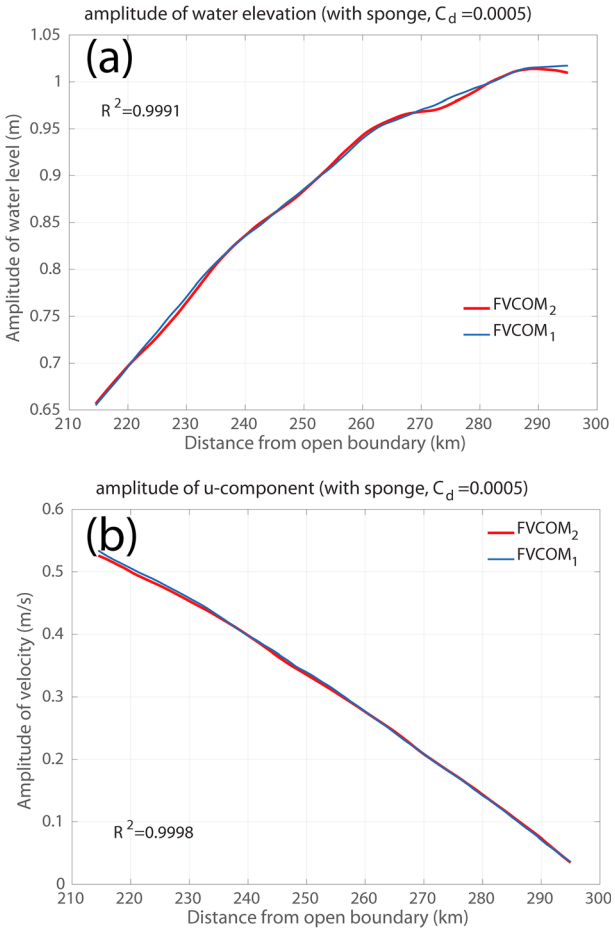

Figure B4. (a) Comparison between the results from the shorter model (red) and those from the longer model (blue) within the shorter model domain for water level amplitude. (b) Same as (a) but for velocity amplitude. FVCOM = Finite Volume Community Ocean Model.

To check the effect of the open boundary condition, we have run a larger domain FVCOM model (Figure B2a), covering the entire Gulf of Mexico (Li et al., 2011). We compare the results from this larger model with those from the smaller model used in this study with the open boundary. The larger model makes the smaller model's open boundary an interior region. For the small domain model, we have applied a sponge layer of 6 km and a coefficient of 0.001; while for the larger Gulf of Mexico model we used a 60-km sponge layer and a coefficient of 0.001. With these treatments, the results show that the open boundary condition for the smaller model does not alter the model results due to significant artificial or computational effects at the boundary. Figures B3a and B3b show the comparison of model results for u and v from the Rigolets (eastern side of the Lake Pontchartrain), one of the major passages for water transport. The red color line is from the original smaller model, while the black line is from the larger domain model that does not have the open boundary at the study area. The low-pass-filtered results are also compared (Figures B3c and B3d) with a 40-hr cutoff period sixth-order Butterworth IIR filter (Emery & Thomson, 2004). They are all consistent with each other.

To further examine the model performance and effect of open boundary, we have also conducted an idealized model experiment to corroborate the conclusion made by the comparison between the large and small models. We use a rectangular model (Figure B2b) of 10 km wide and 300 km long with three solid boundaries in the north, south, and east, and one open boundary in the west (the left end in Figure B2b). The longer model has 27,610 triangles and 14,462 nodes, respectively. The shorter model has 8,291 triangles and 4,348 nodes, respectively. The resolution of these models is ~500 m. The external time steps are ~2 s. An M_2 tide is applied on the open boundary with an amplitude of 1 m. The water depth is 20 m throughout the domain. The bottom drag coefficient is C_d = 0.0005, a rather small value for less friction. We also compare the model results with a linear analytic model with friction. To make sure we do not have appreciable artificial open boundary effect, we apply a sponge layer of 20 km with a coefficient of 0.001 for the long model and 6 km sponge layer for the smaller model with the same coefficient (0.001). The model's ramp-up parameter is chosen as 1 day. The comparison of the results for tidal amplitude along line BC (Figure B2b) is shown in Figure B4a; while the comparison for tidal velocity amplitude along line BC is shown in Figure B4b. We also choose a point within the domain (point P) and compare the time series of the water level (Figure B5a) and velocity (Figure B5b) results from the longer and short models and those from the analytic solution (Li, 1996):

$$\frac{U}{\sqrt{gh_0}} = \frac{\zeta_0}{h_0}\frac{j}{\Phi}\frac{\sin[\phi(1-x/L)]}{\cos(\phi)}, \tag{B4}$$

$$\frac{A}{h_0} = \frac{\zeta_0}{h_0}\frac{\cos[\phi(1-x/L)]}{\cos(\phi)}, \tag{B5}$$

in which U and A are the velocity and water level amplitude at the major tidal frequency, $j = \sqrt{-1}$, and ζ_0, h_0, x, L, and g are the tidal amplitude, mean depth, distance from the open boundary, total length of the channel (Figure B2b), and gravitational acceleration (9.8 m/s^2); the parameters ϕ and Φ and the wavelength are expressed by, respectively,

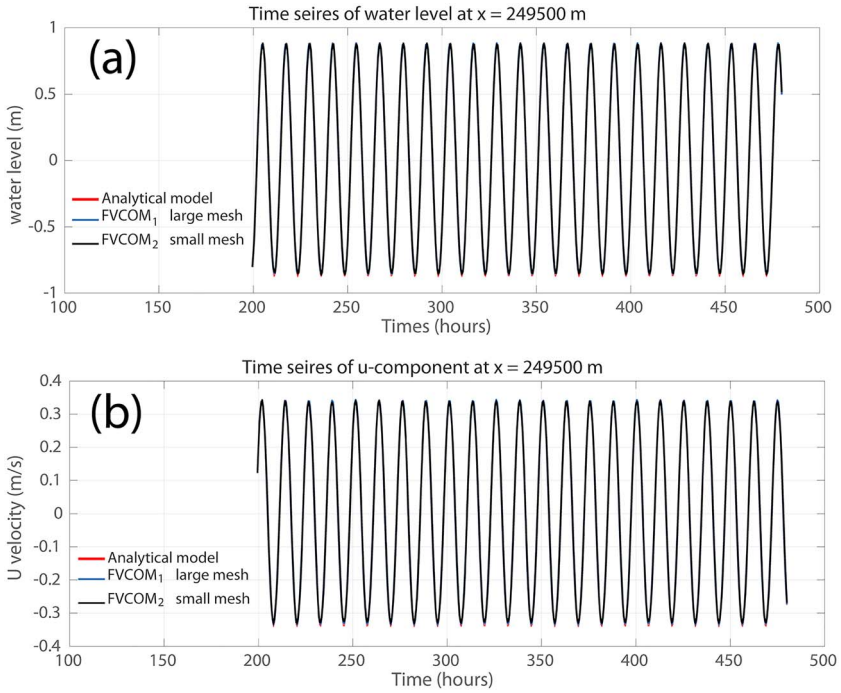

Figure B5. (a) Comparison of time series of water level among the long and short models, as well as the analytic solution at point P. (b) Same as (a) but for velocity. FVCOM = Finite Volume Community Ocean Model.

$$\phi = 2\pi\frac{L}{\lambda}\sqrt{1-j\frac{\beta}{\sigma h_0}},\quad \Phi = \sqrt{1-j\frac{\beta}{\sigma h_0}},\quad \lambda = \frac{2\pi\sqrt{gh_0}}{\sigma}. \tag{B6}$$

The friction coefficient is related to the bottom drag coefficient and provided by

$$\beta = \frac{8C_D}{3\pi}\begin{cases}\dfrac{\zeta_0}{h_0}\sqrt{gh_0}, & \text{if } \left(\dfrac{h_0^2}{C_D\zeta_0 L_0}\right)^{1/3} \geq 1,\\ \dfrac{\zeta_0}{h_0}\sqrt{gh_0}\left(\dfrac{h_0^2}{C_D\zeta_0 L_0}\right)^{1/3}, & \text{if } \left(\dfrac{h_0^2}{C_D\zeta_0 L_0}\right)^{1/3} < 1.\end{cases} \tag{B7}$$

The comparison among the analytic model and the long and short numerical models are summarized by the R^2 values in Table B1. The results verify that the open boundary condition used in this study is reliable for the problem. The model results are not affected by the open boundary.

Table B1
Comparison Among the Analytic, and Long and Short Numerical Models

R^2 of time series	Shorter vs. longer model	Longer FVCOM vs. analytical model
Water elevation	0.9990	0.9995
U component	0.9986	0.9995
R^2 of amplitude	FVCOM1 vs. FVCOM2	Longer FVCOM vs. analytical model
Water elevation	0.9991	0.9980
U component	0.9998	0.9999

Note. FVCOM = Finite Volume Community Ocean Model.

Acknowledgments
The research was supported by NSF (OCE-0554674, DEB-0833225, OCE-1140307, EAR-1139997), and NOAA (NA06OAR4320264-06111039) through the Northern Gulf Institute by NOAA's Office of Ocean and Atmospheric Research. Our computation using the FVCOM was performed on the cluster computer of the Louisiana Optical Network Initiative (LONI) HPC systems at LSU. The authors would like to thank two anonymous reviewers whose comments have resulted to a significantly improved manuscript. Wind data are from NOAA and WAVCIS. All data used in this paper are included in JGR's supporting information.

References

Allen, J. I., Somerfield, P. J., & Gilbert, F. J. (2007). Quantifying uncertainty in high-resolution coupled hydrodynamic-ecosystem models. *Journal of Marine Systems*, *64*(1-4), 3–14. https://doi.org/10.1016/j.jmarsys.2006.02.010

Aoki, K., & Isobe, A. (2007). Application of Finite Volume Coastal Ocean Model to hindcasting the wind-induced sea-level variation in Fukuoka Bay. *Journal of Physical Oceanography*, *63*(2), 333–339. https://doi.org/10.1007/s10872-007-0032-7

Beardsley, R. C., Chen, C., & Xu, Q. (2013). Coastal flooding in Scituate (MA): A FVCOM study of the 27 December 2010 nor'easter. *Journal of Geophysical Research: Oceans*, *118*, 6030–6045. https://doi.org/10.1002/2013JC008862

Beardsley, R. C., & Haidvogel, D. B. (1981). Model studies of the wind-driven transient circulation in the Middle Atlantic Bight. Part 1: Adiabatic boundary conditions. *Journal of Physical Oceanography*, *11*(3), 355–375. https://doi.org/10.1175/1520-0485(1981)011<0355:MSOTWD>2.0.CO;2

Betancourt, R. B., Reyes, E. G., & Da Silveira Mascarenhas, A. Jr. (2008). Subtidal water exchange between Caimanero Lagoon and the adjacent inner shelf, west coast of México: Seasonal circulation pattern and its implication. *Journal of Coastal Research*, *24*(4C), 83–94.

Blumberg, A. F., & Kantha, L. H. (1985). Open boundary condition for circulation models. *Journal of Hydraulic Engineering*, *111*(2), 237–255. https://doi.org/10.1061/(ASCE)0733-9429(1985)111:2(237)

Boas, M. L. (2006). *Mathematical methods in the physical sciences* (p. 839). USA: John Wiley & Sons, Inc.

Boon, J. (2004). *Secrets of the tide: Tide and tidal current analysis and predictions, storm surges and sea level trends* (p. 212). Oxford: Horwood Publishing Ltd.

Brammer, A. J., del Rey, Z. R., Spalding, E. A., & Poirrier, M. A. (2007). Effects of the 1997 bonnet Carré spillway opening on infaunal macro-invertebrates in Lake Pontchartrain, Louisiana. *Journal of Coastal Research*, *235*, 1292–1303. https://doi.org/10.2112/05-0571.1

Cameron, W. M., & Pritchard, a. D. W. (1963). *Estuaries. The sea. M. N. Hill* (pp. 306–324). New York: Wiley.

Carlson, D. F., Muscarella, P. A., Gildor, H., Lipphardt, B. L. Jr., & Fredj, E. (2010). How useful are progressive vector diagrams for studying coastal ocean transport? *Limnology and Oceanography: Methods*, *8*, 98–106.

Casares-Salazar, R., & Mariño-Tapia, I. (2016). Influence of the remote forcing and local winds on the barotropic hydrodynamics of an elongated coastal lagoon. *Journal of Coastal Research*, *32*(1), 116–130.

Chaney, P. L., & Stone, G. W. (1996). Soundside erosion of a nourished beach and implications for winter cold front forcing: West Ship Island, Mississippi. *Oceanographic Literature Review*, *43*(8), 844.

Chapman, D. C. (1985). Numerical treatment of cross-shelf open boundaries in a barotropic coastal ocean model. *Journal of Physical Oceanography*, *15*(8), 1060–1075. https://doi.org/10.1175/1520-0485(1985)015<1060:NTOCSO>2.0.CO;2

Chen, C., Huang, H., Beardsley, R. C., Liu, H., Xu, Q., & Cowles, G. (2007). A finite-volume numerical approach for coastal ocean circulation studies: Comparisons with finite difference models. *Journal of Geophysical Research*, *112*, C03018. https://doi.org/10.1029/2006JC003485

Chen, C., Liu, H., & Beardsley, R. C. (2003). An unstructured grid, finite-volume, three-dimensional, Primitive Equations Ocean Model: Application to coastal ocean and estuaries. *Journal of Atmospheric and Oceanic Technology*, *20*(1), 159–186. https://doi.org/10.1175/1520-0426(2003)020<0159:AUGFVT>2.0.CO;2

Cheng, R. T., Powell, T. M., & Dillon, T. M. (1976). Numerical models of wind-driven circulation in lakes. *Applied Mathematical Modelling*, *1*(3), 141–159. https://doi.org/10.1016/0307-904X(76)90035-4

Chilmakuri, C. S. (2005). Sediment transport and pathogen indicator modeling in Lake Pontchartrain, (PhD Dissertation, 156 pp.). University of New Orleans.

Chuang, W. S., & Swenson, E. M. (1981). Subtidal water level variations in Lake Pontchartrain, Louisiana. *Journal of Geophysical Research*, *86*(C5), 4198–4204. https://doi.org/10.1029/JC086iC05p04198

Chubarenko, B. V., Leitsina, L. V., Esiukova, E. E., & Kurennoy, D. N. (2012). Model analysis of the currents and wind waves in the Vistula Lagoon of the Baltic Sea. *Oceanology*, *52*(6), 748–753. https://doi.org/10.1134/S000143701206001X

Csanady, G. T. (1968). Wind-driven summer circulation in the Great Lakes. *Journal of Geophysical Research*, *73*(8), 2579–2589. https://doi.org/10.1029/JB073i008p02579

Csanady, G. T. (1982). Circulation in the coastal ocean. *Advances in Geophysics*, *23*, 101–184.

de Boer, J. P., & Maas, L. R. (2011). Amplified exchange rate by tidal forcing of a piecewise-linear Helmholtz bay. *Ocean Dynamics*, *61*(12), 2061–2072. https://doi.org/10.1007/s10236-011-0479-3

de Brito, A. N. J., Fragoso, C. R. Jr., & Larson, M. (2018). Tidal exchange in a choked coastal lagoon: A study of Mundaú Lagoon in northeastern Brazil. *Regional Studies in Marine Science*, *17*, 133–142.

De Marchis, M., Ciraolo, G., Nasello, C., & Napoli, E. (2012). Wind- and tide-induced currents in the Stagnone lagoon (Sicily). *Environmental Fluid Mechanics*, *12*(1), 81–100. https://doi.org/10.1007/s10652-011-9225-0

de Oliveira, M. M. F., Ebecken, N. F. F., de Oliveira, J. L. F., & Santos, I. d. A. (2009). Neural network model to predict a storm surge. *Journal of Applied Meteorology and Climatology*, *48*(1), 143–155. https://doi.org/10.1175/2008JAMC1907.1

Duran-Matute, M., Gerkema, T., & Sassi, M. G. (2016). Quantifying the residual volume transport through a multiple-inlet system in response to wind forcing: The case of the western Dutch Wadden Sea. *Journal of Geophysical Research: Oceans*, *121*, 8888–8903. https://doi.org/10.1002/2016JC011807

Elliott, A. J. (1978). Observations of the meteorologically induced circulation in the Potomac Estuary. *Estuarine and Coastal Marine Science*, *6*(3), 285–299. https://doi.org/10.1016/0302-3524(78)90017-8

Emery, W. J., & Thomson, R. E. (2004). *Data analysis methods in physical oceanography* (2nd ed., p. 638). New York: Elsevier.

Engelund, F. (1973). Steady wind set-up in prismatic lakes, reprinted in environmental hydraulics: Stratified flows. In F. B. Pedersen (Ed.), *Lecture Notes on Coastal and Estuarine Studies, 1986*, (Vol. 18, pp. 205–212). New York: Springer.

Feng, Z., & Li, C. (2010). Cold-front-induced flushing of the Louisiana Bays. *Journal of Marine Systems*, *82*(4), 252–264. https://doi.org/10.1016/j.jmarsys.2010.05.015

Fernandes, E. H. L., Marino-Tapia, I., Dyer, K. R., & Moeller, O. O. (2004). The attenuation of tidal and subtidal oscillations in the Patos Lagoon estuary. *Ocean Dynamics*, *54*(3–4), 348–359.

Flather, R. A. (1988). A numerical investigation of tides and diurnal-period continental shelf waves along Vancouver Island. *Journal of Physical Oceanography*, *18*(1), 115–139. https://doi.org/10.1175/1520-0485(1988)018<0115:ANMIOT>2.0.CO;2

Flores, R. P., Rijnsburger, S., Horner-Devine, A. R., Souza, A. J., & Pietrzak, J. D. (2017). The impact of storms and stratification on sediment transport in the Rhine region of freshwater influence. *Journal of Geophysical Research: Oceans*, *122*, 4456–4477. https://doi.org/10.1002/2016JC012362

Forbes, M. J. (1988). Hydrologic investigations of the lower Calcasieu River, Louisiana. U.S. Geological Survey. *Water Resources Investigations Report*, *87-4173*, 61.

Galperin, B., Kantha, L. H., Hassid, S., & Rosati, A. (1988). A quasi-equilibrium turbulent energy model for geophysical flows. *Journal of the Atmospheric Sciences*, *45*(1), 55–62. https://doi.org/10.1175/1520-0469(1988)045<0055:AQETEM>2.0.CO;2

Garvine, R. W. (1985). A simple model of estuarine subtidal fluctuations forced by local and remote wind stress. *Journal of Geophysical Research*, *90*(C6), 11,945–11,948. https://doi.org/10.1029/JC090iC06p11945

Georgiou, I., & McCorquodale, J. A. (2002). Stratification and circulation in Lake Pontchartrain. 140–151.

Georgiou, I. Y. (2002). Three-dimensional hydrodynamic modeling of salinity intrusion and circulation in Lake Pontchartrain, (Doctoral thesis, 171 pp.). New Orleans, LA: University of New Orleans.

Gibbs, M., Abell, J., & Hamilton, D. (2016). Wind forced circulation and sediment disturbance in a temperate lake. *New Zealand Journal of Marine and Freshwater Research*, *50*(2), 209–227. https://doi.org/10.1080/00288330.2015.1116998

Gill, A. (1982). *Atmosphere-ocean dynamics*. New York: Academic Press.

Hamilton, G. D., Soileau, C. W., & Stroud, A. (1982). Numerical modeling study of Lake Pontchartrain. *Journal of the Waterway, Port, Coastal and Ocean Division*, *108*(1), 49–64.

Hansen, D. V., & Rattray, M. Jr. (1965). Gravitational circulation in straits and estuaries. *Journal of Marine Research*, *23*, 104–122.

Hansen, D. V., & Rattray, M. Jr. (1966). New dimensions in estuary classification. *Limnology and Oceanography*, *11*(3), 319–326. https://doi.org/10.4319/lo.1966.11.3.0319

Haralampides, K. (2000). A study of the hydrodynamics and salinity regimes of the Lake Pontchartrain system, (PhD dissertation, 219 pp.). University of New Orleans.

Harris, D. L. (1981). Tides and tidal datums in the United States. U.S. Army Corps of Engineers. *Special Reports*, *7*, 382.

Henriksen, H. J., Troldborg, L., Nyegaard, P., Sonnenborg, T. O., Refsgaard, J. C., & Madsen, B. (2003). Methodology for construction, calibration and validation of a national hydrological model for Denmark. *Journal of Hydrology*, *280*(1-4), 52–71. https://doi.org/10.1016/S0022-1694(03)00186-0

Herrling, G., & Winter, C. (2015). Tidally- and wind-driven residual circulation at the multiple-inlet system East Frisian Wadden Sea. *Continental Shelf Research*, *106*, 45–59. https://doi.org/10.1016/j.csr.2015.06.001

Hill, A. E. (1994). Fortnightly tides in a lagoon with variable choking. *Estuarine, Coastal and Shelf Science*, *38*(4), 423–434. https://doi.org/10.1006/ecss.1994.1029

Horner-Devine, A. R., Hetland, R. D., & MacDonald, D. G. (2015). Mixing and transport in Coastal River plumes. *Annual Review of Fluid Mechanics*, *47*(1), 569–594. https://doi.org/10.1146/annurev-fluid-010313-141408

Huang, H., Chen, C., Cowles, G. W., Winant, C. D., Beardsley, R. C., Hedstrom, K. S., & Haidvogel, D. B. (2008). FVCOM validation experiments: Comparisons with ROMS for three idealized barotropic test problems. *Journal of Geophysical Research*, *113*, C07042. https://doi.org/10.1029/2007JC004557

Huang, W., & Li, C. (2017). Cold front driven flows through multiple inlets of Lake Pontchartrain Estuary. *Journal of Geophysical Research: Oceans*, *122*, 8627–8645. https://doi.org/10.1002/2017JC012977

Jia, P., & Li, M. (2012). Dynamics of wind-driven circulation in a shallow lagoon with strong horizontal density gradient. *Journal of Geophysical Research*, *117*, C01003. https://doi.org/10.1029/2011JC007475

Jordi, A., Basterretxea, G., & Wang, D.-P. (2011). Local versus remote wind effects on the coastal circulation of a microtidal bay in the Mediterranean Sea. *Journal of Marine Systems*, *88*(2), 312–322. https://doi.org/10.1016/j.jmarsys.2011.05.007

Junot, J. A., Poirrier, M. A., & Soniat, T. M. (1983). Effects of saltwater intrusion from the Inner Harbor Navigation Canal on the benthos of Lake Pontchartrain, Louisiana. *Gulf Research Reports*, *7*(3), 247–254.

Keen, T. R. (2002). Waves and currents during a winter cold front in the Mississippi Bight, Gulf of Mexico: Implications for Barrier Island erosion. *Journal of Coastal Research*, *18*(4), 622–636.

Kjerfve, B. (1986). In D. A. Wolfe (Ed.), *Comparative oceanography of coastal lagoons* (pp. 63–81). New York: Estuarine Variability, Academic Press.

Kjerfve, B., & Magill, K. E. (1989). Geographic and hydrodynamic characteristics of shallow coastal lagoons. *Marine Geology*, *88*(3–4), 187–199. https://doi.org/10.1016/0025-3227(89)90097-2

Kolker, A. S., Li, C., Walker, N. D., Pilley, C., Ameen, A. D., Boxer, G., et al. (2014). The impacts of the great Mississippi/Atchafalaya River flood on the oceanography of the Atchafalaya Shelf. *Continental Shelf Research*, *86*, 17–33. https://doi.org/10.1016/j.csr.2014.04.023

Kumar, A., Mishra, D. R., Equeenuddin, S. M., Cho, H. J., & Rastogi, G. (2017). Differential impact of anniversary-severe cyclones on the water quality of a tropical coastal lagoon. *Estuaries and Coasts*, *40*(2), 317–342. https://doi.org/10.1007/s12237-016-0172-3

Lawson, S. E., Wiberg, P. L., McGlathery, K. J., & Fugate, D. C. (2007). Wind-driven sediment suspension controls light availability in a shallow coastal lagoon. *Estuaries and Coasts*, *30*(1), 102–112. https://doi.org/10.1007/BF02782971

Li, C. (1996). Tidally induced residual circulation in estuaries with cross channel bathymetry, (PhD dissertation, 242 pp.). Storrs, CT: University of Connecticut.

Li, C. (2013). Subtidal water flux through a multiple-inlet system: Observations before and during a cold front event and numerical experiments. *Journal of Geophysical Research: Oceans*, *118*, 1877–1892. https://doi.org/10.1002/jgrc.20149

Li, C., Roberts, H., Stone, G. W., Weeks, E., & Luo, Y. (2011). Wind surge and saltwater intrusion in Atchafalaya Bay during onshore winds prior to cold front passage. *Hydrobiologia*, *658*(1), 27–39. https://doi.org/10.1007/s10750-010-0467-5

Li, C., & Valle-Levinson, A. (1999). A two-dimensional analytic tidal model for a narrow estuary of arbitrary lateral depth variation: The intratidal motion. *Journal of Geophysical Research*, *104*(C10), 23,525–23,543. https://doi.org/10.1029/1999JC900172

Li, C., Walker, N., Hou, A., Georgiou, I., Roberts, H., Laws, E., et al. (2008). Circular plumes in Lake Pontchartrain estuary under wind straining. *Estuarine, Coastal and Shelf Science*, *80*(1), 161–172. https://doi.org/10.1016/j.ecss.2008.07.020

Li, C., Weeks, E., & Blanchard, B. W. (2010). Storm surge induced flux through multiple tidal passes of Lake Pontchartrain estuary during Hurricanes Gustav and Ike. *Estuarine, Coastal and Shelf Science*, *87*(4), 517–525. https://doi.org/10.1016/j.ecss.2010.02.003

Li, C., Weeks, E., Huang, W., Milan, B., & Wu, R. (2018). Weather induced transport through a tidal channel calibrated by an unmanned boat. *Journal of Atmospheric and Oceanic Technology*, *35*(2), 261–279. https://doi.org/10.1175/JTECH-D-17-0130.1

Li, C., Weeks, E., & Rego, J. L. (2009). In situ measurements of saltwater flux through tidal passes of Lake Pontchartrain estuary by Hurricanes Gustav and Ike in September 2008. *Geophysical Research Letters*, *36*, L19609. https://doi.org/10.1029/2009GL039802

Lin, J., Li, C., Boswell, K. M., Kimball, M., & Rozas, L. (2016). Examination of winter circulation in a Northern Gulf of Mexico Estuary. *Estuaries and Coasts*, *39*(4), 879–899. https://doi.org/10.1007/s12237-015-0048-y

Maréchal, D. (2004). A soil-based approach to rainfall-runoff modelling in ungauged catchments for England and Wales, (PhD). Cranfield University.

Mellor, G. L., & Yamada, T. (1982). Development of a turbulence closure model for geophysical fluid problem. *Reviews of Geophysics and Space Physics*, *20*(4), 851–875. https://doi.org/10.1029/RG020i004p00851

Moeller, C. C., Huh, O. K., Roberts, H. H., Gumley, L. E., & Menzel, W. P. (1993). Response of Louisiana coastal environments to a coastal front passage. *Journal of Coastal Research*, *9*(2), 434–447.
Mohanty, P. K., & Panda, B. U. S. (2009). Circulation and mixing processes in Chilika lagoon. *Indian Journal of Marine Sciences*, *38*(2), 205–214.
Moller, O., Lorenzzentti, J. A., Stech, J. L., & Mata, M. M. (1996). The Patos Lagoon summertime circulation and dynamics. *Continental Shelf Research*, *16*(3), 335–351. https://doi.org/10.1016/0278-4343(95)00014-R
Orlanski, I. (1976). A simple boundary condition for unbounded hyperbolic flows. *Journal of Computational Physics*, *21*(3), 251–269. https://doi.org/10.1016/0021-9991(76)90023-1
Palma, E. D., & Matano, R. P. (2001). Dynamical impacts associated with radiation boundary conditions. *Journal of Sea Research*, *46*(2), 117–132. https://doi.org/10.1016/S1385-1101(01)00076-4
Parker, B. B. (1984). Frictional effects on the tidal dynamics of shallow estuary, (PhD dissertation, 291 pp.). Baltimore, MD: University of Johns Hopkins.
Pepper, D. A., & Stone, G. W. (2004). Hydrodynamic and sedimentary responses to two contrasting winter storms on the inner shelf of the northern Gulf of Mexico. *Marine Geology*, *210*(1–4), 43–62. https://doi.org/10.1016/j.margeo.2004.05.004
Proudman, J. (1953). *Dynamical oceanography* (p. 409). London: Wiley.
Raymond, W. H., & Kuo, H. L. (1984). A radiation boundary condition for multidimensional flows. *Quarterly Journal of the Royal Meteorological Society*, *110*(464), 535–551. https://doi.org/10.1002/qj.49711046414
Rego, J. L., & Li, C. (2009). On the receding of storm surge along Louisiana's low-lying coast. *Journal of Coastal Research*, *SI*(56), 1045–1049.
Rego, J. L., & Li, C. (2010). Nonlinear terms in storm surge predictions: Effect of tide and shelf geometry with case study from Hurricane Rita. *Journal of Geophysical Research*, *115*, C06020. https://doi.org/10.1029/2009JC005285
Roberts, H. H., Huh, O. K., Hsu, S. A., Rouse, L. J. Jr., & Rickman, D. (1989). Winter storm impacts on the Chenier plain coast of southwestern Louisiana. *Gulf Coast Association of Geological Societies Transactions*, *39*, 515–522.
Roberts, H. H., Walker, N. D., Sheremet, A., & Stone, G. W. (2005). Effects of cold fronts on bayhead delta development: Atchafalaya Bay, Louisiana, USA. In D. M. FitzGerald & J. Knight (Eds.), *High Resolution Marphodynamics and Sedimentary Evolution of Estuaries, Coastal Systems and Continental Margins* (Vol. 8, 269–298). https://doi.org/10.1007/1-4020-3296-X_13
Signell, R. P., & List, J. H. (1997). Modeling waves and circulation in Lake Pontchartrain, Louisiana. Gulf Coast Association of Geological Societies. *Transactions*, *47*, 529–532.
Sikora, W. B., & Kjerfve, B. J. (1985). Factors influencing the salinity regimes of Lake Pontchartrain, Louisiana, a shallow coastal lagoon: Analysis of a long-term data set. *Estuaries*, *8*(2), 170–180. https://doi.org/10.2307/1351866
Smith, N. P. (1985). The decomposition and simulation of the longitudinal circulation in a coastal lagoon. *Estuarine, Coastal and Shelf Science*, *21*(5), 623–632. https://doi.org/10.1016/0272-7714(85)90062-9
Sommerfeld, A., & Straus, E. G. (1967). *Partial differential equations in physics: Lectures on theoretical physics* (Vol. 6). New York: Academic Press.
Sternberger, M. S. (1983). A physical description of long-period net displacement variation within the southern Indian River lagoon, Florida. *Florida Scientist*, *46*(3–4), 396–406.
Swenson, E. M., & Chuang, W. S. (1983). Tidal and subtidal water volume exchange in an estuarine system. *Estuarine, Coastal and Shelf Science*, *16*(3), 229–240. https://doi.org/10.1016/0272-7714(83)90142-7
Tenenbaum, M., & Pollard, H. (1985). *Ordinary differential equations* (p. 808). New York: Dover Publications, Inc.
Umgiesser, G., Ferrarin, C., Cucco, A., De Pascalis, F., Bellafiore, D., Ghezzo, M., & Bajo, M. (2014). Comparative hydrodynamics of 10 Mediterranean lagoons by means of numerical modeling. *Journal of Geophysical Research: Oceans*, *119*, 2212–2226. https://doi.org/10.1002/2013JC009512
Umgiesser, G., Zemlys, P., Erturk, A., Razinkova-Baziukas, A., Mėžinė, J., & Ferrarin, C. (2016). Seasonal renewal time variability in the Curonian Lagoon caused by atmospheric and hydrographical forcing. *Ocean Science*, *12*(2), 391–402. https://doi.org/10.5194/os-12-391-2016
Valle-Levinson, A., Delgado, J. A., & Atkinson, L. P. (2001). Reversing water exchange patterns at the entrance to a semiarid coastal lagoon. *Estuarine, Coastal and Shelf Science*, *53*(6), 825–838. https://doi.org/10.1006/ecss.2000.0813
Valle-Levinson, A., Holderied, K., Li, C., & Chant, R. J. (2007). Subtidal flow structure at the turning region of a wide outflow plume. *Journal of Geophysical Research*, *112*, C04004. https://doi.org/10.1029/2006JC003746
Walker, N. D. (1996). Satellite assessment of Mississippi River plume variability: Causes and predictability. *Remote Sensing of Environment*, *58*(1), 21–35. https://doi.org/10.1016/0034-4257(95)00259-6
Walker, N. D., & Hammack, A. B. (2000). Impacts of winter storms on circulation and sediment transport: Atchafalaya-Vermilion Bay region, Louisiana, USA. *Journal of Coastal Research*, *16*(4), 996–1010.
Waterhouse, A. F., Valle-Levinson, A., & Winant, C. D. (2011). Tides in a system of connected estuaries. *Journal of Physical Oceanography*, *41*(5), 946–959. https://doi.org/10.1175/2010JPO4504.1
Weaver, R. J., Johnson, J. E., & Ridler, M. (2016). Wind-driven circulation in a shallow microtidal estuary: The Indian River Lagoon. *Journal of Coastal Research*, *32*(6), 1333–1343.
Weaver, R. J., Taeb, P., Lazarus, S., Splitt, M., Holman, B. P., & Colvin, J. (2016). Sensitivity of modeled estuarine circulation to spatial and temporal resolution of input meteorological forcing of a cold frontal passage. *Estuarine, Coastal and Shelf Science*, *183*, 28–40. https://doi.org/10.1016/j.ecss.2016.10.014
Weisberg, R. (1976). The Noutidal flow in the Providence River of Narragansett Bay: A stochastic approach to estuarine circulation. *Journal of Physical Oceanography*, *6*(5), 721–734. https://doi.org/10.1175/1520-0485(1976)006<0721:TNFITP>2.0.CO;2
Weisberg, R. H., & Zheng, L. Y. (2006a). Hurricane storm surge simulation for Tampa Bay. *Estuaries and Coasts*, *29*(6), 899–913. https://doi.org/10.1007/BF02798649
Weisberg, R. H., & Zheng, L. Y. (2006b). A simulation of the Hurricane Charley storm surge and its breach of North Captiva Island. Florida. *Scientist*, *69*, 152–165.
White, J. R., Fulweiler, R. W., Li, C., Bargu, S., Walker, N. D., Twilley, R. R., & Green, S. E. (2009). Mississippi River Flood of 2008: Observations of a large freshwater diversion on physical, chemical, and biological characteristics of a shallow estuarine lake. *Environmental Science & Technology*, *43*(15), 5599–5604. https://doi.org/10.1021/es900318t
Wilson, R. E., Wong, K.-C., & Filadelfo, R. (1985). Low frequency sea level variability in the vicinity of the East River tidal strait. *Journal of Geophysical Research*, *90*(C1), 954–960. https://doi.org/10.1029/JC090iC01p00954
Winant, C., Valle-Levinson, A., Ponte, A., Winant, C., Gutierrez-de-velasco, G., & Winters, K. (2014). Observations on the lateral structure of wind-driven flows in a stratified, Semiarid Bay of the Gulf of California. *Estuaries and Coasts*, *37*(6), 1319–1328. https://doi.org/10.1007/s12237-013-9641-0
Wong, K.-C. (1994). On the nature of transverse variability in a coastal plain estuary. *Journal of Geophysical Research*, *99*(C7), 14,209–214,222. https://doi.org/10.1029/94JC00861

Wong, K.-C., & Moses-Hal, J. E. (1998). On the relative importance of the remote and local wind effects to the subtidal variability in a coastal plain estuary. *Journal of Geophysical Research*, *103*(C9), 18,393–18,404. https://doi.org/10.1029/98JC01476

Wong, K.-C., & Wilson, R. E. (1984). Observations of low frequency variability in Great South Bay and relations to atmospheric forcing. *Journal of Physical Oceanography*, *14*(12), 1893–1900. https://doi.org/10.1175/1520-0485(1984)014<1893:OOLFVI>2.0.CO;2

Yuk, J.-h., & Aoki, S.-i. (2009). Effect of wind and rainfall on water exchange in a stratified estuary. *Estuaries and Coasts*, *32*(1), 88–99. https://doi.org/10.1007/s12237-008-9118-8